The Journal of Chemical Physics ARTICLE pubs.aip.org/aip/jcp

Microscopic elasticity from MD. I. Bulk solid and fluid systems

Cite as: J. Chem. Phys. 164, 024110 (2026); doi: 10.1063/5.0303843
Submitted: 24 September 2025 • Accepted: 1 December 2025 •
Published Online: 13 January 2026

View Online Export Citation CrossMark

Andrew L. Lewis,[1] **Benjamin Himberg,**[2] **Alejandro Torres-Sánchez,**[3] **and Juan M. Vanegas**[4,a)]

AFFILIATIONS

[1] Department of Physics, The University of Vermont, Burlington, Vermont 05405, USA
[2] Materials Science Graduate Program, The University of Vermont, Burlington, Vermont 05405, USA
[3] European Molecular Biology Laboratory, Barcelona, Spain
[4] Department of Biochemistry and Biophysics, Oregon State University, Corvallis, Oregon 97331, USA

[a)] **Author to whom correspondence should be addressed:** vanegasj@oregonstate.edu

ABSTRACT

Computational modeling, such as molecular dynamics and Monte Carlo simulations, can be used to estimate the elastic properties of materials through various stress and strain relationships. Here, we demonstrate the effectiveness of the stress–stress fluctuation (SSF) method to estimate the elastic properties of simple van der Waals and molecular materials. The SSF method allows computation of the complete elasticity tensor from a single equilibrium simulation without requiring any type of deformation. While extensively used to characterize the elastic coefficients of crystalline solids and glassy systems, application of the SSF method to fluid systems and biomaterials has been limited. Starting with argon in the solid, liquid, and gas phases, we show that the SSF method gives elastic coefficients and moduli in excellent agreement with values obtained with the explicit deformation and volume fluctuation methods. Comparison of the elastic coefficients and bulk modulus for solid argon with previous computational studies and experimental data provides further validation of our numerical implementation. Beyond argon, we show that the elastic properties of molecular fluids simulated with the coarse-grained MARTINI force-field, which include multi-body interactions such as angle potentials, are also accurately captured by the SSF method. Moreover, the impulsive correction for truncated potentials is essential to obtain accurate values for these fluids and vanishing shear moduli. Our results highlight the broad applicability of the SSF method across a broad range of systems and lay the foundation for its use to characterize the elastic properties of complex molecular systems.

I. INTRODUCTION

The elasticity tensor is a fundamental quantity in continuum mechanics, as it describes the linearized mechanical response, i.e., the stress–strain relationship, in elastic materials. The individual coefficients of the elasticity tensor are often obtained experimentally for a given material or may also be estimated computationally from Monte Carlo or molecular dynamics (MD) simulations.[1–6] Within the context of soft biomaterials such as lipid membranes, elastic moduli of stretching, bending, and tilt play an essential role in describing the energetics of membrane deformation.[7–13] Similar to the bulk and Young's moduli, these macroscopic membrane coefficients have well-defined underpinnings based on the microscopic components of the elasticity tensor.[10–13] Moreover, accurate values of these moduli are important to properly capture the balance between competing phenomena in continuum models of cellular/organellar shape, mechanotransduction, and membrane–protein association, among others.[14–18] However, obtaining elastic coefficients and/or effective moduli of soft materials such as lipid membranes poses a great challenge both experimentally and computationally.[19–21] This is due to various difficulties, including finding deformation methods that individually probe certain modes,[22,23] decoupling equilibrium energetics from viscous dissipation effects,[24–26] and developing theoretical frameworks that can consistently describe both experimental and computational measurements.[20,27–29]

Elastic coefficients of materials can be obtained computationally through a variety of methods, such as (1) explicit deformation (ED), (2) strain (shape) fluctuation, (3) stress fluctuation, or (4) hybrid deformation–fluctuation.[3,4,30–36] In the first method, the material is deformed, and the elastic coefficients are computed from the changes in stress and strain relative to the undeformed configuration. While conceptually simple, the explicit deformation method has various drawbacks, such as having to apply different types of strains to capture the various coefficients, determining an appropriate linear deformation regime, and the inability to decouple individual terms for certain types of material symmetries, as even uniaxial deformations will depend on a combination of elastic coefficients. In the strain (shape) fluctuation method, the material is simulated under an isothermal–isostress $(N\sigma T)$ or isothermal–isobaric (NPT) ensemble, and the elastic coefficients are obtained from the fluctuations in the dimensions of the simulation cell.[3,30] A drawback of this method is that it relies on proper sampling of the phase space of the system by the barostat, which may depend on simulation parameters such as the pressure coupling time constant and material incompressibility for a given algorithm.[37] In the stress–stress fluctuation (SSF) method, the material is typically simulated in the canonical ensemble (NVT), and the elastic coefficients are obtained from three contributions: A kinetic term that depends on the momenta of the particles, the fluctuations in the stress tensor, and the Born term that depends on the first and second derivatives of the potential.[31–34,38] Having to compute the second derivatives of the potential is a drawback of the SSF method. This motivated the development of the hybrid deformation–fluctuation method, which uses deformations to estimate the Born term and only requires knowledge of the first derivatives of the potential.[36,39] The SSF method has a long history that includes early work by Born, Huang, and others[31,40,41] to characterize the elasticity of crystalline materials at low temperatures by explicitly defining the elasticity tensor from the internal potential energy of the system (see Barron and Klein[31] for a more detailed discussion). Squire *et al.*[1] later extended the theory by defining the elasticity tensor starting from the Helmholtz or canonical free energy and showing that at finite temperatures, fluctuations in the stress provide a significant contribution to the overall values. General expressions for the SSF formula in the various thermodynamic ensembles are given by Bavaud *et al.*[32] A key advantage of the SSF method is the ability to obtain all elastic coefficients from a single equilibrium simulation at constant volume. Computing the so-called Born term of the elasticity tensor, which depends on the first and second derivatives of the potential, requires that the potential can be decomposed into central pairwise terms.[38,42] Multi-body potentials that are often defined in terms of angles or dihedrals must be written in terms of pairwise distances.[43–47]

The application of the SSF method has been largely focused on solid (crystalline) and glassy systems.[1,4–6,33–36,39,43,44,48] Early work on cross-linked polymers[49,50] suggested that this method may not be suitable to estimate the elasticity of fluid-like systems due to a lack of convergence and inherent stability issues.[51] However, it is unclear if those studies[49,50] adequately included the impulsive corrections[5] needed to accurately compute the Born term from the truncated Lennard-Jones potential. A more recent study by Lips and Maass[52] computed the local elasticity tensor for a coarse-grained (CG) lipid membrane using Monte Carlo simulations. Here, we present an extensive MD simulation study demonstrating the effectiveness of the SSF method to estimate the elastic properties of soft materials such as molecular liquids. We show that the SSF formula produces elastic coefficients for argon in the solid, liquid, and gas phases in excellent agreement compared to other methods and consistent with theoretical expectations of material stability. Furthermore, we show that the impulsive correction for truncated potentials is essential to obtain accurate elastic coefficients, especially for liquids. We carefully consider the convergence of the method for different systems and provide criteria for efficient sampling. We also characterize the elastic coefficients of molecular liquids based on the popular coarse-grained MARTINI[53] force-field, which includes bonded 3-body interactions such as harmonic angle potentials. Our results show that the SSF method is a powerful tool to characterize the elastic properties of solids and soft materials from MD simulations. We further explore the application of the SSF method to characterize the elastic properties of liquid–liquid interfaces and lipid membranes in our companion paper.[54]

II. THEORY

A. Stress and elasticity tensors from the canonical free energy

To obtain the elasticity tensor from MD simulations, we follow the derivation provided by Tadmor and Miller[38] (Chap. 8) and start by considering the canonical free energy of the system, A. This free energy describes the total mechanical energy of our molecular system and serves as the strain energy density within the context of continuum mechanics. The Cauchy stress tensor, $\boldsymbol{\sigma}$, can be obtained by finding the change in the free energy with respect to a deformation

$$\boldsymbol{\sigma} = \frac{\partial A}{\partial \boldsymbol{\epsilon}} \qquad \text{or} \qquad \sigma_{ij} = \frac{\partial A}{\partial \epsilon_{ij}}. \tag{1}$$

Here, the deformation is represented by the infinitesimal strain or small strain tensor, $\boldsymbol{\epsilon}$, which may be expressed vectorially or in index notation with lowercase Roman indices determining the type of spatial deformation. Similarly, the elasticity tensor, $\boldsymbol{c}$, is defined as the change in the Cauchy stress with respect to another independent spatial deformation,

$$\boldsymbol{c} = \frac{\partial^2 A}{\partial \boldsymbol{\epsilon} \partial \boldsymbol{\epsilon}} = \frac{\partial \boldsymbol{\sigma}}{\partial \boldsymbol{\epsilon}} \qquad \text{or} \qquad c_{ijkl} = \frac{\partial^2 A}{\partial \epsilon_{kl} \partial \epsilon_{ij}} = \frac{\partial \sigma_{ij}}{\partial \epsilon_{kl}}. \tag{2}$$

The canonical, or Helmholtz, free energy is classically defined as

$$A = -\frac{1}{\beta} \ln(Z), \tag{3}$$

where Z is the canonical partition function and $\beta = \frac{1}{k_B T}$. The partition function is defined in terms of the system's Hamiltonian, H, as

$$Z = \frac{1}{h^{3N} N_A! N_B! \dots} \int \exp\left(-\beta H(\boldsymbol{r}, \boldsymbol{p})\right) d\boldsymbol{r} d\boldsymbol{p}, \tag{4}$$

where h is Planck's constant; $\boldsymbol{r} = \left(\boldsymbol{r}^1, \dots, \boldsymbol{r}^\alpha, \dots, \boldsymbol{r}^N\right)$ and $\boldsymbol{p} = \left(\boldsymbol{p}^1, \dots, \boldsymbol{p}^\alpha, \dots, \boldsymbol{p}^N\right)$ are the positions and momenta of the particles, respectively; N_X is the number of particles of species X;

and $N = \sum_X N_X$. The Hamiltonian of a system of N interacting classical particles subject to a potential, $U(\boldsymbol{r}^\alpha)$, is defined as

$$H(\boldsymbol{r},\boldsymbol{p}) = \sum_{\alpha}^{N} \frac{|\boldsymbol{p}^\alpha|^2}{2m^\alpha} + U(\boldsymbol{r}^\alpha). \tag{5}$$

In order to obtain the Cauchy stress or elasticity tensors from Eq. (3), we must take derivatives of the partition function with respect to the strain tensor. To do this, we make use of finite strain theory and the deformation gradient, $\boldsymbol{F}$, which is a two-point tensor that defines how changes of a material point in a reference configuration correspond to changes in the same material point in the deformed configuration.

In the reference configuration, the coordinates of the particles are given by $\boldsymbol{R}^\alpha$ (or R_I^α) and $\boldsymbol{P}^\alpha$ (or P_I^α), while in the deformed configuration they are given by $\boldsymbol{r}^\alpha$ (or r_i^α) and $\boldsymbol{p}^\alpha$ (or p_i^α). The deformation gradient is then defined as

$$F_{i,J} = \frac{\partial r_i}{\partial R_J}, \tag{6}$$

where the lowercase Roman indices refer to the spatial coordinates of the deformed configuration and the uppercase Roman indices refer to the material coordinates in the reference configuration. Additional relations and identities involving the deformation gradient, including mappings for the particle momenta, are included in Appendix A. Note that the reference configuration need not be an equilibrium state, and the deformed configuration could be any other state. This mapping is also independent of the choice of coordinates, which do not need to be orthogonal. We now proceed to define the first Piola–Kirchhoff stress, the energy conjugate of the deformation gradient, as

$$\Pi_{iJ} = \frac{1}{V_0}\frac{\partial A}{\partial F_{i,J}} = \frac{-1}{V_0 \beta Z}\frac{\partial Z}{\partial F_{i,J}}. \tag{7}$$

The first Piola–Kirchhoff stress is related to the Cauchy stress by

$$\sigma_{ij} = \frac{1}{\det(\boldsymbol{F})} F_{j,J}\Pi_{iJ}, \tag{8}$$

where $\det(\boldsymbol{F})$ is the ratio of the volume of the deformed configuration to the volume of the reference configuration [see Eq. (A17) in Appendix A]. Similarly, we can define the mixed elasticity tensor D_{iJkL} by taking the derivative of the first Piola–Kirchhoff stress with respect to the deformation gradient,

$$D_{iJkL} = \frac{\partial \Pi_{iJ}}{\partial F_{k,L}} = \frac{1}{V_0}\frac{\partial^2 A}{\partial F_{k,L}\partial F_{i,J}} = \frac{1}{V_0\beta Z}\left(\frac{1}{Z}\frac{\partial Z}{\partial F_{k,L}}\frac{\partial Z}{\partial F_{i,J}} - \frac{\partial^2 Z}{\partial F_{k,L}\partial F_{i,J}}\right). \tag{9}$$

Note that both Π_{iJ} and D_{iJkL} are two-point tensors. The elasticity tensor is then obtained through a transformation from the mixed elasticity tensor and the Cauchy stress,

$$c_{ijkl} = \frac{1}{\det(\boldsymbol{F})} F_{j,J} F_{l,L} D_{iJkL} - \delta_{ik}\sigma_{jl}. \tag{10}$$

To obtain both Π_{iJ} and D_{iJkL}, we must take derivatives of the partition function with respect to the deformation gradient, which requires a canonical transformation of the Hamiltonian coordinates r_i^α and p_i^α. A new Hamiltonian $\hat{H}$ can be generated by using the deformation gradient,

$$\hat{H}(\boldsymbol{R},\boldsymbol{P};\boldsymbol{F}) = \sum_{\alpha}^{N} \frac{1}{2m^\alpha}(\boldsymbol{F}^{-T}\boldsymbol{P}^\alpha)_i(\boldsymbol{F}^{-T}\boldsymbol{P}^\alpha)_j\delta_{ij} + U(\boldsymbol{F}\boldsymbol{R}^\alpha), \tag{11}$$

where $R_I^\alpha = F_{I,j}^{-1} r_j^\alpha$ and $P_I^\alpha = F_{I,j} p_j^\alpha$. This transformed Hamiltonian is equivalent to the untransformed one, as it preserves the symplectic structure of Hamilton's equations. We can use the transformed Hamiltonian to define the derivative of the partition function with respect to the deformation gradient,

$$\frac{\partial Z}{\partial F_{i,J}} = -\frac{\beta}{h^{3N}N_A!N_B!\dots}\int \frac{\partial \hat{H}(\boldsymbol{R},\boldsymbol{P};\boldsymbol{F})}{\partial F_{i,J}} \exp\left(-\beta\hat{H}(\boldsymbol{R},\boldsymbol{P};\boldsymbol{F})\right) d\boldsymbol{R}d\boldsymbol{P}. \tag{12}$$

Noting that the canonical expectation value can be defined as

$$\begin{aligned}\langle Q\rangle &= \frac{1}{Zh^{3N}N_A!N_B!\dots}\int Q(\boldsymbol{r},\boldsymbol{p})\exp\left(-\beta H(\boldsymbol{r},\boldsymbol{p})\right)\,d\boldsymbol{r}d\boldsymbol{p}\\ &= \frac{1}{Zh^{3N}N_A!N_B!\dots}\int Q(\boldsymbol{R},\boldsymbol{P};\boldsymbol{F})\exp\left(-\beta\hat{H}(\boldsymbol{R},\boldsymbol{P};\boldsymbol{F})\right)\,d\boldsymbol{R}d\boldsymbol{P},\end{aligned} \tag{13}$$

we can write the derivative of the partition function with respect to the deformation gradient in terms of the transformed Hamiltonian as

$$\frac{\partial Z}{\partial F_{i,J}} = -\beta Z\left\langle \frac{\partial \hat{H}}{\partial F_{i,J}}\right\rangle, \tag{14}$$

which allows us to write the first Piola–Kirchhoff stress as

$$\Pi_{i,J} = \frac{1}{V_0}\left\langle \frac{\partial \hat{H}}{\partial F_{i,J}}\right\rangle. \tag{15}$$

We can similarly write the mixed elasticity tensor in terms of the transformed Hamiltonian as follows:

$$\begin{aligned}D_{iJkL} &= \frac{\partial}{\partial F_{k,L}}\left(\frac{1}{V_0}\left\langle\frac{\partial\hat{H}}{\partial F_{i,J}}\right\rangle\right) = \frac{1}{V_0 Zh^{3N}N_A!N_B!\dots}\int\\ &\quad\times \frac{\partial^2\hat{H}}{\partial F_{k,L}\partial F_{i,J}}\exp(-\beta\hat{H})\,d\boldsymbol{R}d\boldsymbol{P} - \frac{\beta}{V_0Zh^{3N}N_A!N_B!\dots}\\ &\quad\times\int\frac{\partial\hat{H}}{\partial F_{k,L}}\frac{\partial\hat{H}}{\partial F_{i,J}}\exp(-\beta\hat{H})\,d\boldsymbol{R}d\boldsymbol{P} + \frac{\beta}{V_0(Zh^{3N}N_A!N_B!\dots)^2}\\ &\quad\times\left[\int\frac{\partial\hat{H}}{\partial F_{k,L}}\exp(-\beta\hat{H})\,d\boldsymbol{R}d\boldsymbol{P}\int\frac{\partial\hat{H}}{\partial F_{i,J}}\exp(-\beta\hat{H})\,d\boldsymbol{R}d\boldsymbol{P}\right]\\ &= \frac{1}{V_0}\left[\left\langle\frac{\partial^2\hat{H}}{\partial F_{i,J}\partial F_{k,L}}\right\rangle - \beta\left(\left\langle\frac{\partial\hat{H}}{\partial F_{i,J}}\frac{\partial\hat{H}}{\partial F_{k,L}}\right\rangle - \left\langle\frac{\partial\hat{H}}{\partial F_{i,J}}\right\rangle\left\langle\frac{\partial\hat{H}}{\partial F_{k,L}}\right\rangle\right)\right].\end{aligned} \tag{16}$$

To compute the first and second derivatives of $\hat{H}$ with respect to the deformation gradient, we must consider the corresponding derivatives of the potential U. Assuming that interatomic potentials are conservative scalar functions of the particle positions,[38,42] which is true for most classical potentials used in MD simulations, we can replace the potential $U(\boldsymbol{r}^\alpha)$ with a sum of central pairwise potential terms $\mathring{U}(r^{\alpha\beta})$ such that

$$U(\boldsymbol{r}^\alpha) = \sum_{\beta\neq\alpha} \mathring{U}(r^{\alpha\beta}), \tag{17}$$

where $\boldsymbol{r}^{\alpha\beta} = \boldsymbol{r}^\beta - \boldsymbol{r}^\alpha$ and $r^{\alpha\beta} = |\boldsymbol{r}^{\alpha\beta}|$ is the distance between the pair of interacting particle pairs α and β. Such a change in the description of the potential implies that the first derivatives of the potential, i.e., the net forces acting on the particles, can be decomposed into sums of central pairs,

$$\frac{\partial U}{\partial r_i^\alpha} = -\sum_{\beta\neq\alpha} \frac{\partial \mathring{U}}{\partial r^{\alpha\beta}} \frac{r_i^{\alpha\beta}}{r^{\alpha\beta}}. \tag{18}$$

An N-body potential can, in general, be decomposed into $\frac{1}{2}N(N-1)$ possible pairs.[38,42,46,47] Similarly, we must consider the position of two possibly independent particles, $\boldsymbol{r}^\alpha$ and $\boldsymbol{r}^\gamma$, to obtain the second derivatives of the potential. These two particles would be the same in the case of a two-body potential but may be different in the case of three-body or higher order multi-body potentials. As such, the substitution of the original potential with a sum of pairwise terms in the second derivative requires a double sum over the pairs $\{\alpha,\beta\}$ and $\{\gamma,\xi\}$ to obtain

$$\begin{aligned}\frac{\partial}{\partial r_j^\gamma}\left(\frac{\partial U}{\partial r_i^\alpha}\right) &= \sum_{\gamma\neq\xi}\frac{\partial}{\partial r^{\gamma\xi}}\left(-\sum_{\beta\neq\alpha}\frac{\partial \mathring{U}}{\partial r^{\alpha\beta}}\frac{r_i^{\alpha\beta}}{r^{\alpha\beta}}\right)\frac{\partial r^{\gamma\xi}}{\partial r_j^\gamma},\\ \frac{\partial^2 U}{\partial r_j^\gamma \partial r_i^\alpha} &= \sum_{\alpha\neq\beta}\sum_{\gamma\neq\xi}\frac{\partial^2 \mathring{U}}{\partial r^{\gamma\xi}\partial r^{\alpha\beta}}\frac{r_i^{\alpha\beta}}{r^{\alpha\beta}}\frac{r_j^{\gamma\xi}}{r^{\gamma\xi}} + \sum_{\alpha\neq\beta}\frac{\partial \mathring{U}}{\partial r^{\alpha\beta}}\frac{1}{r^{\alpha\beta}}\left(\delta_{ij} - \frac{r_i^{\alpha\beta} r_j^{\alpha\beta}}{r^{\alpha\beta 2}}\right).\end{aligned} \tag{19}$$

Armed with the first and second derivatives of the potential, we can proceed to compute the first and second derivatives of the Hamiltonian, giving expressions for $\Pi_{i,J}$ [Eq. (15)] and D_{iJkL} [Eq. (16)], and consequently σ_{ij} [Eq. (8)] and c_{ijkl} [Eq. (10)].

The first derivative of the Hamiltonian with respect to the deformation gradient can be written as

$$\frac{\partial \hat{H}}{\partial F_{i,J}} = \sum_\alpha \frac{\partial}{\partial F_{i,J}}\left(\frac{1}{2m^\alpha}p_q^\alpha p_q^\alpha + U(\boldsymbol{r}^\alpha)\right) \tag{20}$$

$$= \sum_\alpha\left(\frac{1}{m^\alpha}\frac{\partial p_q^\alpha}{\partial F_{i,J}}p_q^\alpha + \frac{\partial U}{\partial r_q^\alpha}\frac{\partial r_q^\alpha}{\partial F_{i,J}}\right) \tag{21}$$

$$= \sum_\alpha\left(\frac{-1}{m^\alpha}F_{J,q}^{-1}p_q^\alpha p_i^\alpha + \frac{\partial U}{\partial r_q^\alpha}R_J^\alpha\delta_{qi}\right), \tag{22}$$

which allows us to write the first Piola–Kirchhoff stress as

$$\Pi_{iJ} = \frac{1}{V_0}\left\langle\frac{\partial \hat{H}}{\partial F_{i,J}}\right\rangle = \frac{1}{V_0}\sum_\alpha\left\langle\frac{-1}{m^\alpha}F_{J,q}^{-1}p_q^\alpha p_i^\alpha + \frac{\partial U}{\partial r_i^\alpha}R_J^\alpha\right\rangle. \tag{23}$$

We can further manipulate the second term in the equation above by recalling that the first derivative of the potential can be expressed in terms of pairwise distances [see Eq. (18)] such that

$$\sum_\alpha \frac{\partial U}{\partial r_i^\alpha}R_J^\alpha = -\sum_{\alpha\neq\beta}\frac{\partial \mathring{U}}{\partial r^{\alpha\beta}}\frac{r_i^{\alpha\beta}}{r^{\alpha\beta}}R_J^\alpha. \tag{24}$$

Noting that $r_i^{\alpha\beta} = -r_i^{\beta\alpha}$ and $R_J^{\alpha\beta} = R_J^\beta - R_J^\alpha$, we can write the second term in Eq. (20) as

$$\begin{aligned}-\sum_{\alpha\neq\beta}\frac{\partial \mathring{U}}{\partial r^{\alpha\beta}}\frac{r_i^{\alpha\beta}}{r^{\alpha\beta}}R_J^\alpha &= -\frac{1}{2}\left(\sum_{\alpha\neq\beta}\frac{\partial \mathring{U}}{\partial r^{\alpha\beta}}\frac{r_i^{\alpha\beta}}{r^{\alpha\beta}}R_J^\alpha + \sum_{\beta\neq\alpha}\frac{\partial \mathring{U}}{\partial r^{\beta\alpha}}\frac{r_i^{\beta\alpha}}{r^{\beta\alpha}}R_J^\beta\right)\\ &= -\frac{1}{2}\left(\sum_{\alpha\neq\beta}\frac{\partial \mathring{U}}{\partial r^{\alpha\beta}}\frac{r_i^{\alpha\beta}}{r^{\alpha\beta}}R_J^\alpha - \sum_{\beta\neq\alpha}\frac{\partial \mathring{U}}{\partial r^{\alpha\beta}}\frac{r_i^{\alpha\beta}}{r^{\alpha\beta}}R_J^\beta\right)\\ &= \sum_{\substack{\alpha,\beta\\ \beta>\alpha}}\frac{\partial \mathring{U}}{\partial r^{\alpha\beta}}\frac{r_i^{\alpha\beta}}{r^{\alpha\beta}}R_J^{\alpha\beta},\end{aligned} \tag{25}$$

where the factor of 1/2 in the last line is folded into the double sum over the two particles α and β by specifying that $\beta > \alpha$, which avoids over-counting pairs. We can insert this relation into the first Piola–Kirchhoff stress [Eq. (23)] to obtain

$$\Pi_{iJ} = \frac{1}{V_0}\left\langle -\sum_\alpha \frac{1}{m^\alpha}F_{J,q}^{-1}p_q^\alpha p_i^\alpha + \sum_{\substack{\alpha,\beta\\ \beta>\alpha}}\frac{\partial \mathring{U}}{\partial r^{\alpha\beta}}\frac{r_i^{\alpha\beta}}{r^{\alpha\beta}}R_J^{\alpha\beta}\right\rangle, \tag{26}$$

which is then used to obtain the well-known equation for the Cauchy stress,

$$\sigma_{ij} = \frac{1}{V}\left\langle -\sum_\alpha \frac{p_i^\alpha p_j^\alpha}{m^\alpha} + \sum_{\substack{\alpha,\beta\\ \beta>\alpha}}\frac{\partial \mathring{U}}{\partial r^{\alpha\beta}}\frac{r_i^{\alpha\beta}r_j^{\alpha\beta}}{r^{\alpha\beta}}\right\rangle. \tag{27}$$

Following a similar approach, the second derivative of the Hamiltonian with respect to the deformation gradient can be written as

$$\begin{aligned}\frac{\partial^2 \hat{H}}{\partial F_{i,J}\partial F_{k,L}} &= \sum_\alpha \frac{1}{m^\alpha}\left(\frac{\partial^2 p_q^\alpha}{\partial F_{i,J}\partial F_{k,L}}p_q^\alpha + \frac{\partial p_q^\alpha}{\partial F_{i,J}}\frac{\partial p_q^\alpha}{\partial F_{k,L}}\right)\\ &\quad + \frac{\partial^2 U}{\partial r_q^\gamma \partial r_s^\alpha}\frac{\partial r_q^\alpha}{\partial F_{i,J}}\frac{\partial r_s^\gamma}{\partial F_{k,L}} + \frac{\partial U}{\partial r_q^\alpha}\frac{\partial^2 r_q^\alpha}{\partial F_{i,J}\partial F_{k,L}}\\ &= \sum_\alpha \frac{1}{m^\alpha}\Big(F_{L,i}^{-1}F_{J,q}^{-1}p_q^\alpha p_k^\alpha + F_{J,k}^{-1}F_{L,q}^{-1}p_q^\alpha p_i^\alpha\\ &\quad + F_{J,q}^{-1}F_{L,q}^{-1}p_i^\alpha p_k^\alpha\Big) + \frac{\partial^2 U}{\partial r_i^\gamma \partial r_k^\alpha}R_J^\gamma R_L^\alpha.\end{aligned} \tag{28}$$

In the second to last term above, the second derivative of the potential can be replaced with sums over pairwise terms [see Eq. (19)], as was done a few steps earlier in Eqs. (24) and (25),

$$\begin{aligned}\frac{\partial^2 U}{\partial r_i^\gamma \partial r_k^\alpha}R_J^\gamma R_L^\alpha &= \sum_{\alpha\neq\beta}\sum_{\gamma\neq\xi}\frac{\partial^2 \mathring{U}}{\partial r^{\gamma\xi}\partial r^{\alpha\beta}}\frac{r_k^{\alpha\beta}}{r^{\alpha\beta}}\frac{r_i^{\gamma\xi}}{r^{\gamma\xi}}R_J^\gamma R_L^\alpha\\ &\quad + \sum_{\alpha\neq\beta}\frac{\partial \mathring{U}}{\partial r^{\alpha\beta}}\frac{1}{r^{\alpha\beta}}\left(\delta_{ik} - \frac{r_i^{\alpha\beta}r_k^{\alpha\beta}}{r^{\alpha\beta 2}}\right)R_J^\alpha R_L^\alpha\\ &= \sum_{\substack{\alpha,\beta\\ \beta>\alpha}}\sum_{\substack{\gamma,\xi\\ \xi>\gamma}}\frac{\partial^2 \mathring{U}}{\partial r^{\gamma\xi}\partial r^{\alpha\beta}}\frac{r_k^{\alpha\beta}}{r^{\alpha\beta}}\frac{r_i^{\gamma\xi}}{r^{\gamma\xi}}R_J^{\gamma\xi}R_L^{\alpha\beta}\\ &\quad + \sum_{\substack{\alpha,\beta\\ \beta>\alpha}}\frac{\partial \mathring{U}}{\partial r^{\alpha\beta}}\frac{1}{r^{\alpha\beta}}\left(\delta_{ik} - \frac{r_i^{\alpha\beta}r_k^{\alpha\beta}}{r^{\alpha\beta 2}}\right)R_J^{\alpha\beta}R_L^{\alpha\beta}.\end{aligned} \tag{29}$$

In the first term of the double sum above, we first iterate over the particle pair $\{\alpha, \beta\}$ and then iterate over a second potentially independent pair $\{\gamma, \xi\}$.

The SSF formula for the spatial elasticity tensor is obtained by combining Eqs. (10), (16), and (28),

$$c_{ijkl} = c^{0}_{ijkl} + c^{\mathrm{F}}_{ijkl} + c^{\mathrm{K}}_{ijkl}, \tag{30}$$

$$c^{0}_{ijkl} = \frac{1}{V}\left\langle \sum_{\substack{\alpha,\beta \\ \beta>\alpha}} \sum_{\substack{\gamma,\xi \\ \xi>\gamma}} \frac{\partial^2 \mathring{U}}{\partial r^{\gamma\xi}\partial r^{\alpha\beta}} \frac{r_i^{\alpha\beta} r_j^{\alpha\beta} r_k^{\gamma\xi} r_l^{\gamma\xi}}{r^{\alpha\beta} r^{\gamma\xi}} - \sum_{\substack{\alpha,\beta \\ \beta>\alpha}} \frac{\partial \mathring{U}}{\partial r^{\alpha\beta}} \frac{r_i^{\alpha\beta} r_j^{\alpha\beta} r_k^{\alpha\beta} r_l^{\alpha\beta}}{(r^{\alpha\beta})^3} \right\rangle, \tag{31}$$

$$c^{\mathrm{F}}_{ijkl} = -\beta V\left(\langle \sigma^{\mathrm{inst}}_{ij} \sigma^{\mathrm{inst}}_{kl} \rangle - \sigma_{ij}\sigma_{kl}\right), \tag{32}$$

$$c^{\mathrm{K}}_{ijkl} = \frac{1}{V}\left\langle \sum_{\alpha} \frac{1}{m^{\alpha}} \left(\delta_{il} p_j^{\alpha} p_k^{\alpha} + \delta_{jk} p_i^{\alpha} p_l^{\alpha} + \delta_{jl} p_i^{\alpha} p_k^{\alpha} + \delta_{ik} p_j^{\alpha} p_l^{\alpha}\right) \right\rangle. \tag{33}$$

The so-called Born term, c^{0}_{ijkl}, corresponds to the adiabatic elasticity at $T = 0$ K, and it represents the intrinsic elastic response of the material due to interatomic interactions. The fluctuation term, c^{F}_{ijkl}, corresponds to the covariance of the stress tensor, which is determined by the energy fluctuations within the material. Note that $\sigma^{\mathrm{inst}}_{ij}$ in Eq. (32) corresponds to the instantaneous value of the stress for any given system configuration and not the ensemble average. Finally, the kinetic term, c^{K}_{ijkl}, is obtained from the momenta of the particles in the system. In general, the Born term tends to have positive values, while the fluctuation term tends to be negative.

Classical molecular systems are often parameterized using bonded potentials such as harmonic bonds (2-body), harmonic or cosine angles (3-body), and harmonic or cosine dihedrals (4-body), among many others. Any 3-body or higher order potentials must be carefully included in the Born term [Eq. (31)], as we need to cast the potentials in terms of pairwise distances.[38,43,44] For a harmonic angle potential acting on particles α, β, and γ, one can define the potential and its derivatives explicitly in terms of pairwise distances ($r^{\alpha\beta}$, $r^{\alpha\gamma}$, and $r^{\beta\gamma}$) using various identities, including the dot product and law of cosines (see the supplementary material). Once the first and second derivatives of the 3-body angle potential have been obtained, one must then incorporate nine different contributions into the first term of Eq. (31), which correspond to the three homo-pairs $\{r^{\alpha\beta}, r^{\alpha\beta}\}$, $\{r^{\alpha\gamma}, r^{\alpha\gamma}\}$, and $\{r^{\beta\gamma}, r^{\beta\gamma}\}$ as well as the six hetero-pairs $\{r^{\alpha\beta}, r^{\alpha\gamma}\}$, $\{r^{\alpha\gamma}, r^{\alpha\beta}\}$, $\{r^{\alpha\beta}, r^{\beta\gamma}\}$, $\{r^{\beta\gamma}, r^{\alpha\beta}\}$, $\{r^{\alpha\gamma}, r^{\beta\gamma}\}$, and $\{r^{\beta\gamma}, r^{\alpha\gamma}\}$. Note that swapping the order of the hetero-pairs produces different contributions to the Born term even though the second derivatives of the potential are interchangeable due to Schwarz's theorem, e.g.,

$$\frac{\partial^2 \mathring{U}}{\partial r^{\beta\gamma}\partial r^{\alpha\beta}} = \frac{\partial^2 \mathring{U}}{\partial r^{\alpha\beta}\partial r^{\beta\gamma}}. \tag{34}$$

Definitions of all the bonded and non-bonded interatomic potentials used in this study, including their first and second derivatives, are provided in the supplementary material.

In general, the elasticity tensor has $81 = 3^4$ individual terms. However, this number can be reduced through various minor (e.g., $c_{xyxy} = c_{yxxy}$) and major (e.g., $c_{xxyy} = c_{yyxx}$) symmetries to 21 unique elements for bulk materials, which can be written as a symmetric 6×6 stiffness matrix,

$$c_{mn} = \begin{bmatrix} c_{11} & c_{12} & c_{13} & c_{14} & c_{15} & c_{16} \\ c_{12} & c_{22} & c_{23} & c_{24} & c_{25} & c_{26} \\ c_{13} & c_{23} & c_{33} & c_{34} & c_{35} & c_{36} \\ c_{14} & c_{24} & c_{34} & c_{44} & c_{45} & c_{46} \\ c_{15} & c_{25} & c_{35} & c_{45} & c_{55} & c_{56} \\ c_{16} & c_{26} & c_{36} & c_{46} & c_{56} & c_{66}, \end{bmatrix} \tag{35}$$

using the following compact Voigt notation:

Tensor index:	xx	yy	zz	yz	xz	xy
Voigt index:	1	2	3	4	5	6

For systems with isotropic or cubic symmetry, the stiffness matrix reduces to

$$c_{mn} = \begin{bmatrix} c_{11} & c_{12} & c_{12} & 0 & 0 & 0 \\ c_{12} & c_{11} & c_{12} & 0 & 0 & 0 \\ c_{12} & c_{12} & c_{11} & 0 & 0 & 0 \\ 0 & 0 & 0 & c_{44} & 0 & 0 \\ 0 & 0 & 0 & 0 & c_{44} & 0 \\ 0 & 0 & 0 & 0 & 0 & c_{44} \end{bmatrix}, \tag{36}$$

where $c_{44} = \frac{1}{2}(c_{11} - c_{12})$ for the isotropic case.

B. Compliance and elastic moduli

The values of the elasticity tensor obtained with the SSF formula [Eq. (30)] correspond to the coefficients in an unstressed state where $\sigma_{ij} = 0$. However, the coefficients obtained from stress–strain relations, i.e., Hooke's law, will differ for systems where $\sigma_{ij} \neq 0$.[31,32,44,55–57] The incremental change in Cauchy stress around a pre-stressed configuration is not determined solely by the material modulus c_{ijkl} but must also include additional terms that depend explicitly on the initial stress σ_{ij}.[56,57] This is because the stress rate must be taken in an objective sense using the Truesdell rate.[38] For an infinitesimal strain increment ϵ_{kl} relative to the pre-stressed configuration, the change in stress is given by

$$\Delta\sigma_{ij} = [c_{ijkl} + \sigma_{jl}\delta_{ik} + \sigma_{jk}\delta_{il} - \sigma_{ij}\delta_{kl}]\epsilon_{kl}, \tag{37}$$

where summations are carried out over repeated Roman indices. This relation can be cast into the standard form $\Delta\sigma_{ij} = \tilde{c}_{ijkl}\epsilon_{kl}$, where the effective tangent modulus $\tilde{c}_{ijkl}$ incorporates both the material stiffness and the geometric contributions due to the pre-stress. By symmetrizing the stress–strain contractions, we obtain a relation for the elasticity tensor under a finite Cauchy stress,

$$\tilde{c}_{ijkl} = c_{ijkl} + \frac{1}{2}[\sigma_{ik}\delta_{jl} + \sigma_{il}\delta_{jk} + \sigma_{jk}\delta_{il} + \sigma_{jl}\delta_{ik} - 2\sigma_{ij}\delta_{kl}]. \tag{38}$$

Following Wallace,[56] we refer to the elements of $\tilde{c}_{ijkl}$ as stress–strain coefficients (also known as Birch coefficients[56,58]), as they are the effective values that would be obtained by explicitly deforming the material experimentally or computationally. The values of c_{ijkl} and $\tilde{c}_{ijkl}$ are only significantly different for systems under high pressure or for gases, where the elastic coefficients are of the order of the Cauchy stress. In addition, note that $\tilde{c}_{ijkl}$ only fulfills major symmetries under conditions of hydrostatic loading.

While individual elastic coefficients may be obtained experimentally or computationally, it is also common to measure moduli such as the Young's modulus for uniaxial deformations or the bulk modulus for isotropic volume changes. These moduli can be readily defined in terms of the individual elastic coefficients by means of the compliance tensor, s_{ijkl}, which relates strain to stress in the inverse of Hooke's law, $\epsilon_{ij} = s_{ijkl}\Delta\sigma_{kl}$. The individual compliance coefficients can be obtained from the elasticity tensor through

$$\tilde{c}_{ijkl}s_{klpq} = s_{ijkl}\tilde{c}_{klpq} = \frac{1}{2}(\delta_{ip}\delta_{jq} + \delta_{iq}\delta_{jp}), \tag{39}$$

or from the stiffness matrix in Voigt notation,

$$\tilde{c}_{mn}s_{np} = s_{mn}\tilde{c}_{np} = \delta_{mp}. \tag{40}$$

Note that the coefficients in s_{mn} are, in general, not equal to the corresponding s_{ijkl} because of the number of times a given s_{mn} appears in Eq. (40). However, they follow these simple relations,[57]

$$s_{ijkl} = s_{mn} \quad \text{if} \quad m, \quad n = 1,2,3, \tag{41a}$$

$$s_{ijkl} = \frac{1}{2}s_{mn} \text{ if } m = 1,2,3,\ n = 4,5,6, \text{ and if } m = 4,5,6,\ n = 1,2,3, \tag{41b}$$

$$s_{ijkl} = \frac{1}{4}s_{mn} \text{ if } m,\ n = 4,5,6. \tag{41c}$$

Starting with an orthonormal set of vectors $\{\boldsymbol{x},\boldsymbol{y},\boldsymbol{z}\}$ such that $\delta_{ij} = x_i x_j + y_i y_j + z_i z_j$, the Young's modulus, $\tilde{E}_z$, and bulk modulus, $\tilde{B}$, can be defined as follows:[59]

$$\frac{1}{\tilde{E}_z} = \tilde{s}_{ijkl}z_i z_j z_k z_l, \tag{42}$$

$$\frac{1}{\tilde{B}} = \tilde{s}_{ijkl}(x_i x_j + y_i y_j + z_i z_j)(x_k x_l + y_k y_l + z_k z_l). \tag{43}$$

The Poisson ratio can be similarly defined as

$$\nu_{zy} = -\tilde{E}_z\tilde{s}_{ijkl}z_i z_j y_k y_l, \tag{44}$$

where $\boldsymbol{z}$ defines the direction of extension and $\boldsymbol{y}$ defines the direction of transverse deformation. Putting it all together, we obtain the well-known formulas for the Young's modulus, bulk modulus, and Poisson ratio for isotropic/cubic materials,

$$\tilde{E} = \frac{(\tilde{c}_{11} + 2\tilde{c}_{12})(\tilde{c}_{11} - \tilde{c}_{12})}{\tilde{c}_{11} + \tilde{c}_{12}}, \tag{45}$$

$$\tilde{B} = \frac{\tilde{c}_{11} + 2\tilde{c}_{12}}{3}, \tag{46}$$

$$\nu = \frac{\tilde{c}_{12}}{\tilde{c}_{11} + \tilde{c}_{12}}. \tag{47}$$

Given that it is not always possible to compare computational values of the bulk modulus with experiments, we compare the values obtained with the SSF formula with two other methods: Explicit deformation and volume fluctuations. In the explicit deformation method, one measures the bulk modulus from the change in the hydrostatic stress, $\sigma_h = \frac{1}{3}\mathrm{tr}(\boldsymbol{\sigma})$, as the volume strain, $\epsilon_V = \mathrm{tr}(\boldsymbol{\epsilon})$, changes due to an applied hydrostatic pressure,

$$\tilde{B}^{\mathrm{ED}} = \frac{\partial\sigma_h}{\partial\epsilon_V}. \tag{48}$$

In the volume fluctuation method, the system is simulated in the isothermal–isobaric ensemble, *NPT*, and the bulk modulus is obtained from the fluctuations in the volume

$$\tilde{B}^{\mathrm{VF}} = -\langle V\rangle\left(\frac{\partial\langle V\rangle}{\partial P}\right)^{-1} = \frac{k_B T\langle V\rangle}{\langle V^2\rangle - \langle V\rangle^2}. \tag{49}$$

III. MD SIMULATION METHODS

Molecular dynamics (MD) simulations were performed with the GROMACS simulation package v2020.[60] A custom version of the GROMACS-LS software,[45–47,61] which integrates GROMACS with the MDStress library, was used to run simulations to estimate the elastic coefficients using Eq. (30). Lennard-Jones 6-12 parameters, $\sigma = 0.34$ nm and $\epsilon = 0.988\,97$ kJ/mol, for the argon systems were obtained from Horton and Leech.[1,62] The MARTINI 3.0 force-field[53] was used for all the coarse-grained (CG) liquid systems. Long-range Lennard-Jones interactions using the 6-12 potential were truncated using different treatments. For simulations used in Secs. IV A and IV B, the Lennard-Jones potential was truncated using a smooth switching function starting at a switching value of $r_{\mathrm{sw}} = 1.4$ nm and going to zero at $r_{\mathrm{cut}} = 1.5$ nm. For the remainder of the simulations (Secs. IV C and IV D), the Lennard-Jones potential was truncated using a plain cutoff with a shift at $r_{\mathrm{cut}} = 1.1$ nm. See the supplementary material for definitions of the Lennard-Jones potential and the switching function. Other important simulation parameters for all the solid and liquid systems are provided in Table I. Newton's equations of motion were integrated using the leapfrog algorithm with a time step Δt. Temperature was held constant using the velocity rescaling thermostat of Bussi *et al.*[63] with a coupling time constant τ_T. For constant pressure simulations, the pressure was maintained isotropically with the cell rescaling barostat of Bernetti and Bussi[37] with a coupling time constant τ_P. For all systems, an initial solid or liquid configuration was first energy minimized and then equilibrated under constant temperature and pressure for a total time t_{equil}. This was followed by a production run also at constant temperature and pressure for a total time t_{prod}, storing the particle positions and velocities at every 5 ps. From this *NPT* production run, a simulation frame was extracted that most closely matched the average box dimensions/volume. This box average frame was then used to setup five independent simulation replicas with different initial velocities to compute the elasticity tensor. Each replica was simulated at constant volume (*NVT*) for a total time of t_{elast}. The elastic coefficients

TABLE I. Selected simulation parameters for atomistic argon and CG MARTINI systems.

	Atomistic argon			CG MARTINI			
	Solid	Liquid	Gas	Butane	Octane	Dodecane	Water
Temperature (K)	40	100	300	310	310	310	310
Pressure (MPa)	0.1	1.0	2.5	2.0	0.1	0.1	0.1
Avg. Vol. (nm^3)	110.6	147.6	4764	505.5	535.6	481.9	436.1
No. of particles	2916	2916	2916	3600	4320	3993	3564
Δt (ps)	0.002	0.002	0.002	0.005	0.005	0.005	0.005
τ_T (ps)	0.4	0.4	0.4	1.0	1.0	1.0	1.0
τ_P (ps)	4.0	4.0	4.0	5.0	5.0	5.0	5.0
NPT t_{equil} (ns)	2	2	2	50	50	50	50
NPT t_{prod} (ns)	25	25	25	1000	1000	1000	1000
NVT t_{elast} (ns)[a]	5 × 150	5 × 150	5 × 150	5 × 2500	5 × 2500	5 × 2500	5 × 2500
NVT t_{ED} (ns)[b]	19 × 100	19 × 100	19 × 100	19 × 1000	19 × 1000	19 × 1000	19 × 1000

[a] Elastic coefficients obtained from 5 independent replicas with different initial conditions.

[b] Explicit deformation bulk modulus obtained from 19 simulations at different deformations.

c_{mn} for each system were obtained from the average of the five replicas while also averaging over equivalent elements of the stiffness matrix (e.g., $c_{11} = c_{22} = c_{33}$).

The time-series of the volume during the NPT production runs was used to determine the bulk modulus for all systems using Eq. (49). When obtaining the bulk modulus using the volume fluctuation method from an isothermal–isobaric (NPT) simulation, one must ensure that the pressure coupling algorithm samples the correct region of the volume phase space, as this can have large effects on the computed modulus even if the method is well converged. As such, the pressure and temperature coupling must be performed at every simulation step regardless of the pressure or temperature coupling algorithms used or the coupling time constants (τ_P and τ_T). In particular, for GROMACS, this translates to setting the following simulation input parameters: `nsttcouple = 1`, `nstpcouple = 1`, and `verlet-buffer-tolerance = 0.0005`. Incorrect calculation of the instantaneous pressure in CG systems due to improper setting of parameters for generating neighbor lists has been recently reported by Kim *et al.*[64]

The bulk modulus was also computed from explicit deformation (ED) simulations by computing the change in the hydrostatic stress relative to the change in volume [Eq. (48)]. For this method, a set of 19 frames were extracted from the NPT production trajectory, which spans the range of the 10th to 90th percentile (p) of the simulation volumes computed over the length of the trajectory. One frame was extracted that matched the average volume ($p = 0.50$), while 9 frames were uniformly extracted in each of the compressive ($0.10 \le p < 0.50$) and expansive ($0.50 < p \le 0.90$) regimes. Each of these ED simulations was run under constant volume and temperature (NVT) for a total time t_{ED}. The bulk modulus for the compressive and expansive regimes was independently computed and then averaged to obtain the final values of $\tilde{B}^{\text{ED}}$. All data analysis and plots were created using the Python NumPy, SciPy, and Matplotlib libraries.[65–67]

IV. RESULTS AND DISCUSSION

A. Convergence of the stress–stress fluctuation method

We first analyze the time dependence of the elastic coefficients obtained from the SSF formula for solid ($T = 40$ K) and liquid ($T = 100$ K) argon to determine the optimal strategy for convergence. We use the autocorrelation function ($\text{ACF}(t) = \langle f(t_0) f(t_0 + t) \rangle_{t_0}$) of the pressure tensor ($P_{ij} = -\sigma_{ij}$), computed from short 5 ns NVT simulations while saving the pressure tensor at every time step, to estimate the timescale for adequate sampling intervals. The time-series of the diagonal, P_{ii}, and off-diagonal, P_{ij}, elements of the pressure tensor, as well as their corresponding ACFs, are shown in Fig. S1 for solid argon. The characteristic autocorrelation times were obtained from fitting the ACFs to a simple exponential function of the form $\exp(-t/\tau)$. For solid argon, the ACFs decay rapidly, and the autocorrelation times are $\tau_{ii} = 0.34$ ps and $\tau_{ij} = 0.23$ ps, which are in the order of 150 time steps. The time-series of the pressure tensor and ACFs for liquid argon are shown in Fig. S2. The autocorrelation times for liquid argon have similar values in the range of 0.2–0.3 ps.

Figure 1 shows the convergence of the three non-zero elastic coefficients (c_{11}, c_{12}, and c_{44}) for solid argon using sampling intervals of 0.02 ps [panels (a)–(c)], 1.0 ps [panels (d)–(f)], and 2.0 ps [panels (g)–(i)]. Three independent runs, each 150 ns long, with different initial conditions, were simulated at the given sampling interval. While, at the shortest sampling interval of 0.02 ps, the stress at each frame is not expected to be completely uncorrelated, the various elastic coefficients consistently converge after ~50 ns or ~2.5×10^6 samples. For the longer sampling intervals of 1.0 and 2.0 ps, 3–8 times higher than the pressure autocorrelation time, the elastic coefficients appear to consistently converge after a similar number of samples ~5×10^4, which correspond to different simulation times. Although the variance between independent runs is higher for the larger sampling intervals, the average final values

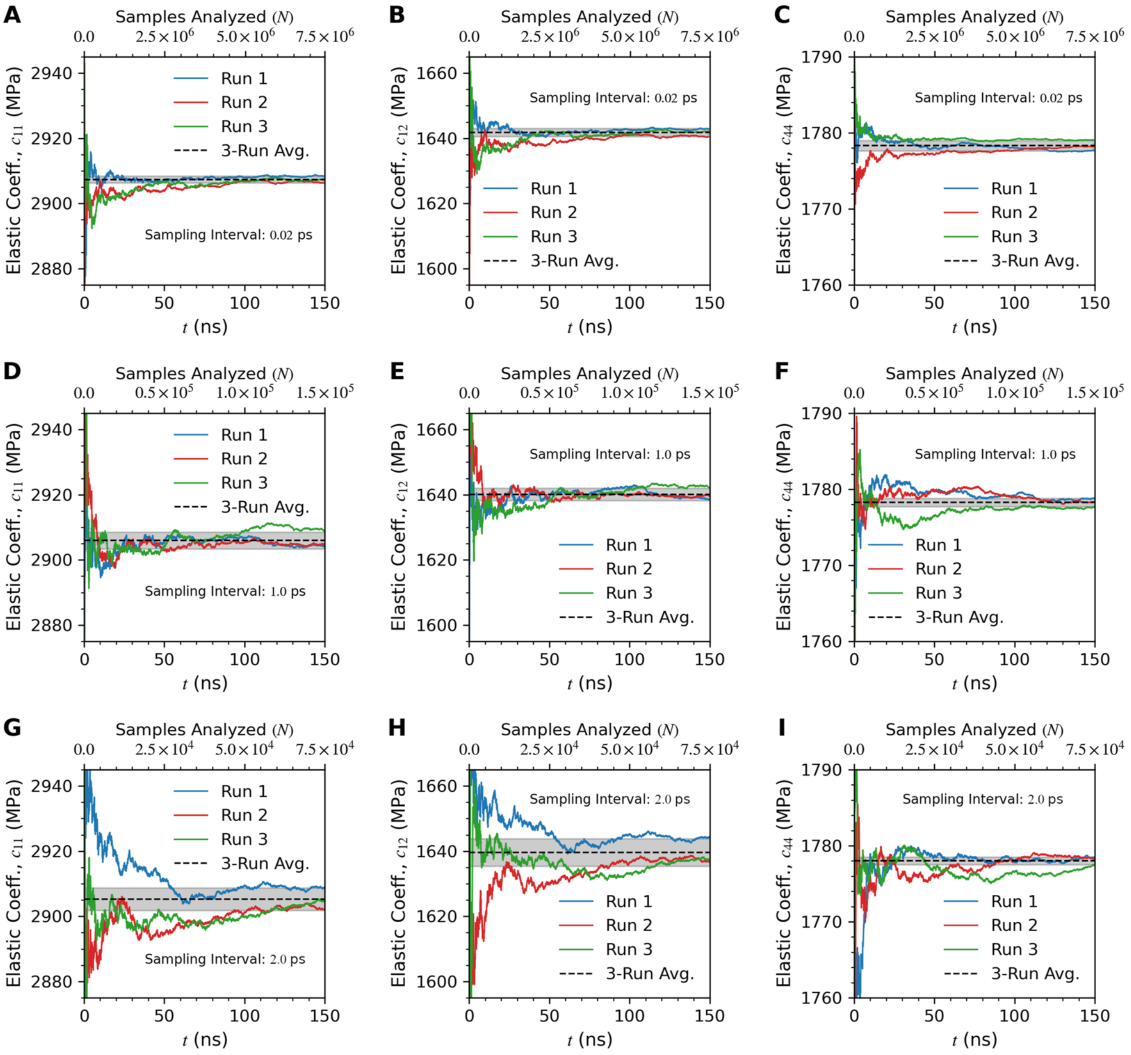

FIG. 1. Convergence of elastic coefficients for solid argon using different sampling intervals. The top row [(a)–(c)] uses a sampling interval of 0.02 ps, the middle row [(d)–(f)] uses a sampling interval of 1.0 ps, and the bottom row [(g)–(i)] uses a sampling interval of 2.0 ps. Left panels show c_{11}, middle panels show c_{12}, and right panels show c_{44}. Three independent simulations with different initial conditions were run at each sampling interval shown in blue, red, and green. The dashed black line shows the 3-run average value at the end of the simulations, while the gray shaded region shows the standard deviation.

of the elastic coefficients are within error of each other (see Table S1). A similar convergence analysis for liquid argon is shown in Fig. S3 using sampling intervals of 0.02, 0.2, and 1.0 ps with three independent simulation runs of 300 ns for each interval. The pattern of convergence for the liquid argon systems shows very similar trends to those observed for the solid phase, except that a larger number of samples ($\sim 1 \times 10^5$) is needed to achieve a similar level of convergence. As with the solid system, the average final values of the elastic coefficients for liquid argon are within error of each other (see Table S2), regardless of the sampling interval, as long as a sufficient number of simulation frames are analyzed.

B. Elasticity of solid, liquid, and gaseous argon

Having established the convergence of the SSF method for both solid and liquid argon systems in Sec. IV A, we now present an extensive analysis of the elastic properties of argon in various phases and provide comparisons with other computational methods as well as experimental data. Table II shows a compendium of elastic coefficients (including the individual contributions from the Born, fluctuation, and kinetic terms), Poisson ratios, and bulk moduli for argon. In the case of solid argon (T = 40 K), the Born term is the dominating contribution for all three elastic coefficients (c_{11}, c_{12}, and c_{44}), while the fluctuation term softens the response

TABLE II. Elastic properties of argon in the solid, liquid, and gas phases.

	Solid	Liquid	Gas
P (MPa)	0.08 ± 0.03	0.95 ± 0.04	2.501 ± 0.002
T (K)	40.001 ± 0.001	100.02 ± 0.04	300.01 ± 0.01
ρ (Kg/m^3)	1749	1311	40.6
c_{11} ($\tilde{c}_{11}$) (MPa)[a]	2906 ± 3 (2906)	321 ± 3 (320)	4.98 ± 0.04 (2.48)
Born	3690.89 ± 0.05	2240.75 ± 0.06	1.776 ± 0.001
Fluct.	−843 ± 3	−2029 ± 3	−6.94 ± 0.04
Kin.	58.219 ± 0.003	109.030 ± 0.005	10.137 ± 0.001
c_{12} ($\tilde{c}_{12}$) (MPa)	1640 ± 2 (1640)	320 ± 5 (321)	−0.03 ± 2 (2.48)
Born	2110.52 ± 0.02	746.93 ± 0.03	0.5919 ± 0.0002
Fluct.	−470 ± 2	−427 ± 5	−0.62 ± 0.02
Kin.	0.0 ± 0.0	0.0 ± 0.0	0.0 ± 0.0
c_{44} ($\tilde{c}_{44}$) (MPa)	1778 ± 1 (1778)	1.1 ± 0.7 (0.1)	2.50 ± 0.02 (0.00)
Born	2110.52 ± 0.02	746.93 ± 0.03	0.592 ± 0.001
Fluct.	−362.7 ± 0.2	−800.4 ± 0.6	−3.16 ± 0.02
Kin.	29.109 ± 0.002	54.515 ± 0.003	5.068 ± 0.001
ν[b]	0.3608 ± 0.0001	0.501 ± 0.002	0.501 ± 0.002
$\tilde{B}$ (MPa)[c]	2062 ± 2	320 ± 4	2.475 ± 0.004
$\tilde{B}^{\text{ED}}$ (MPa)[d]	2064 ± 2	322 ± 2	2.474 ± 0.004
$\tilde{B}^{\text{VF}}$ (MPa)[e]	2140 ± 70	320 ± 50	2.47 ± 0.08

[a] Data inside the box are computed through the SSF method [Eq. (30)].

[b] Obtained from $\tilde{c}_{11}$ and $\tilde{c}_{12}$ using Eq. (47).

[c] Obtained from $\tilde{c}_{11}$ and $\tilde{c}_{12}$ using Eq. (46).

[d] Computed through the explicit deformation method using Eq. (48).

[e] Computed through the volume fluctuation method using Eq. (49).

by 17%–23% due to its negative values. The kinetic contribution is less than 2% for the solid at this temperature. All three elastic coefficients are independent of each other for the cubic argon solid, and the stability of the material must obey the following three conditions:

$$M_1 = \tilde{c}_{11} + 2\tilde{c}_{12} \geq 0, \tag{50}$$

$$M_2 = \tilde{c}_{44} \geq 0, \tag{51}$$

$$M_3 = \tilde{c}_{11} - \tilde{c}_{12} \geq 0, \tag{52}$$

where $\tilde{c}_{mn}$ are the stress–strain elastic coefficients [see Eq. (38)] that take into account the net stress acting on the system (e.g., from hydrostatic loading). The stability criteria are determined by finding the eigenvalues of the elasticity tensor under the constraint that the tensor must be positive definite.[44,51] For solid argon, we find that the stability conditions are satisfied as $M_1 = 6186 \pm 6$, $M_2 = 1778 \pm 1$, and $M_3 = 1266 \pm 1$.

The bulk modulus for solid argon, $\tilde{B} = 2062 \pm 2$ MPa, obtained from Eq. (46) using the stress–strain elastic coefficients $\tilde{c}_{11}$ and $\tilde{c}_{12}$ is in excellent agreement with the value obtained from the explicit deformation method, $\tilde{B}^{\text{ED}} = 2064 \pm 2$ MPa. The explicit deformation bulk modulus $\tilde{B}^{\text{ED}}$ [see Eq. (48)] was obtained from small volume changes (<0.2% for the solid) that are well within the linear deformation regime [see Fig. S4(a)]. An alternate measurement of the bulk modulus obtained from the fluctuations in the system volume [$\tilde{B}^{\text{VF}} = 2140 \pm 70$ MPa, see Eq. (49)] of an equilibrium isothermal–isobaric simulation is also in good agreement, although the estimated error in that value is much higher. The Poisson ratio, obtained from c_{11} and c_{12} using Eq. (47), has a value of 0.36 for the solid, which is in good agreement with typical values expected for crystalline solids near 0.3.

In Fig. 2, we compare the values of c_{11}, c_{12}, c_{44}, and $\tilde{B}$ to experimental values obtained from speed of sound measurements[68–70] for a range of temperatures up to 80 K. The simulations for these solid systems are conducted at a pressure of 0.1 MPa, and therefore the c_{mn} and $\tilde{c}_{mn}$ coefficients are indistinguishable. Note that many of the original experimental observations correspond to the adiabatic elastic coefficients, which must be converted to their isothermal counterparts. To do this, one must first obtain the compliance matrix, $s_{mn} = c_{mn}^{-1}$, followed by a conversion from adiabatic to isothermal values using the following relation:

$$s_{mn}^{\text{IsoT}} = s_{mn}^{\text{Adia}} + \alpha_m \alpha_n \frac{T}{C_p}, \tag{53}$$

where α_m is the thermal strain coefficient and C_p is the specific heat capacity at constant pressure. For crystalline materials with cubic symmetry, only one thermal strain coefficient is needed as $\alpha_1 = \alpha_2 = \alpha_3$ and $\alpha_4 = \alpha_5 = \alpha_6 = 0$ (see Epishin and Lisovenko[71]). The isothermal values of c_{mn} can then be obtained by inversion of the isothermal compliance matrix. While all the values of the elastic coefficients and bulk modulus (blue squares) obtained with the SSF method show a linear response from 10 to 80 K, the experimental measurements (black lines) only begin to show linearity above 30 K

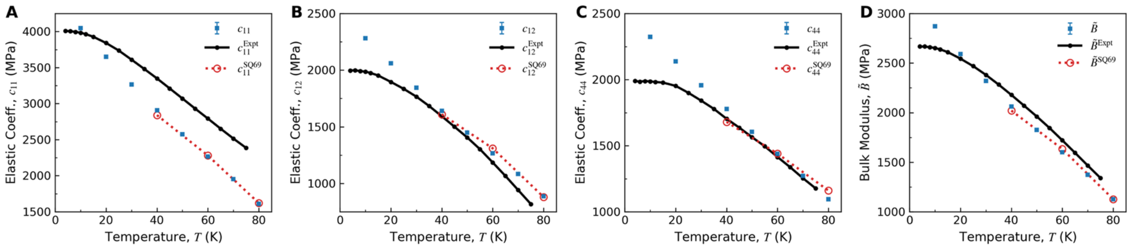

FIG. 2. Comparison of isothermal elastic properties of solid argon for a range of temperatures up to 80 K. Panels (a)–(c) show the elastic coefficients c_{11}, c_{12}, and c_{44}, respectively, while panel (d) shows the bulk modulus. Results obtained with the SSF formula from this work are shown as blue squares. Computational results from Monte Carlo simulations from Squire *et al.*[1] (SQ69) are shown as red circles. Experimental values obtained from speed of sound measurements[68–70] are shown in black lines.

(Fig. 2). At temperatures below 30 K quantum effects change the elastic response of the material, which cannot be properly captured with a simple two-body Lennard-Jones potential and would require 3-body or higher order terms.[72,73] Compared to experiments at 40 K, the value of c_{11} is underestimated by 13%, while the values of c_{12}, c_{44}, and $\tilde{B}$ are all within a margin of 6%. For completeness, Fig. 2 also includes results from an earlier Monte Carlo simulation study by Squire *et al.*[1] (red circles), which also used the SSF method and the same Lennard-Jones parameters by Horton and Leech.[62] The data from Squire *et al.* are in excellent agreement with our calculations, as both sets of results largely overlap each other.

Continuing with the analysis of liquid argon at $T = 100$ K, we observe a drastic reduction in the value of $c_{11} = 321 \pm 3$ MPa compared to 2906 ± 3 MPa in the solid phase. As the material expands in the lower density liquid, there is a 39% decrease in the Born term, while the fluctuation term more than doubles, resulting in these two contributions largely canceling each other out (Table II). The value of $c_{12} = 320 \pm 5$ MPa is indistinguishable from c_{11}, and the stress–strain shear modulus is effectively zero ($\tilde{c}_{44} = 0.1 \pm 0.7$ MPa) as expected for an isotropic liquid ($\tilde{c}_{44} = 0$ is the stability condition for an isotropic liquid). Note that the sum of the Born and kinetic terms for c_{44} has a large value, 801.4 MPa, that is completely canceled by the fluctuation term so that the shear modulus vanishes. The Poisson ratio $(\nu = 0.501 \pm 0.002)$ is also in excellent agreement with the expected ideal liquid value of 0.5. The SSF bulk modulus ($\tilde{B} = 320 \pm 4$ MPa) for the liquid is also nearly identical to the values obtained from the explicit deformation [$\tilde{B}^{\mathrm{ED}} = 322 \pm 2$, see Fig. S4(b)] and volume fluctuation ($\tilde{B}^{\mathrm{VF}} = 320 \pm 50$) methods.

In the case of the argon gas, we find that the elastic coefficients and their corresponding Born, fluctuation, and kinetic contributions are orders of magnitude smaller due to the low density of the gas (Table II). The value of the stress–strain shear modulus ($\tilde{c}_{44}$) is zero, similarly to the liquid argon case. As expected for a gas, the value of $\tilde{B} = 2.475 \pm 0.004$ MPa is very close to the applied pressure of $P = 2.501 \pm 0.002$ MPa. The values of the volume fluctuation and explicit deformation bulk modulus are in excellent agreement with the value obtained from the SSF method for the argon gas. The Poisson ratio for the argon gas obtained with Eq. (47) gives a value of 0.501 ± 0.002 as expected from the indistinguishable stress–strain coefficients, $\tilde{c}_{11} = \tilde{c}_{12} = 2.48$ MPa. However, it is clear from the elastic coefficient $c_{12} = -0.02 \pm 2$ MPa that the gas is perfectly compressible and, therefore, the Poisson ratio should vanish.[74] This likely indicates that Eq. (47), derived for isotropic solids, is not adequate for gases.

C. Truncated potentials and impulsive correction

MD simulations often employ long-range potentials such as Lennard-Jones and electrostatics, which extend to infinity. In the case of the Lennard-Jones potential, which converges more rapidly at long distances, it is common practice to modify the functional form through various schemes such that the potential goes to zero at a given cutoff distance. All the argon systems presented in Secs. IV A and IV B have been simulated using a switching scheme where the potential is multiplied by a switching function that ensures that the potential decreases smoothly to zero at the given cutoff of 1.5 nm (see Sec. III). Another approach is to simply truncate the potential at the cutoff value while also shifting the potential so that it is exactly zero at the cutoff distance. Truncating the potential at the cutoff creates discontinuities in the energy and any of its derivatives, which can significantly affect the Born term of the elasticity tensor. Let us consider a potential interaction between particles α and β that is truncated and shifted at r_{cut},

$$U_{\mathrm{HScut}}(r^{\alpha\beta}) = \Big(U(r^{\alpha\beta}) - U(r_{\mathrm{cut}})\Big)\Big(1 - H(r^{\alpha\beta} - r_{\mathrm{cut}})\Big), \tag{54}$$

where H is the Heaviside function. The first derivative of Eq. (54) with respect to the particle distance $r^{\alpha\beta}$ can be written as

$$\frac{\partial U_{\mathrm{HScut}}(r^{\alpha\beta})}{\partial r^{\alpha\beta}} = \left(\frac{\partial U(r^{\alpha\beta})}{\partial r^{\alpha\beta}}\right)\Big(1 - H(r^{\alpha\beta} - r_{\mathrm{cut}})\Big) + \Big(U(r_{\mathrm{cut}}) - U(r^{\alpha\beta})\Big)\delta(r^{\alpha\beta} - r_{\mathrm{cut}}), \tag{55}$$

where we have used the so-called weak derivative identity $H'(x - x_0) = \delta(x - x_0)$. The last term in Eq. (55) is usually ignored, as the Dirac delta function, which is non-zero only at r_{cut}, is effectively canceled by the shifted potential that equals zero at r_{cut}. This impulsive term from the Dirac delta function does not vanish in the case of truncated potentials that are not shifted and must be properly included in the stress and elasticity formulas. Upon taking a second derivative with respect to $r^{\alpha\beta}$, one finds additional terms that are non-vanishing,

$$\begin{aligned}\frac{\partial^2 U_{\mathrm{HScut}}}{\partial r^{\alpha\beta 2}} &= \left(\frac{\partial^2 U}{\partial r^{\alpha\beta 2}}\right)\left(1 - H(r^{\alpha\beta} - r_{\mathrm{cut}})\right)\\ &\quad - 2\left(\frac{\partial U(r^{\alpha\beta})}{\partial r^{\alpha\beta}}\right)\delta(r^{\alpha\beta} - r_{\mathrm{cut}})\\ &\quad + \left(U(r_{\mathrm{cut}}) - U(r^{\alpha\beta})\right)\left(\frac{\partial \delta(r^{\alpha\beta} - r_{\mathrm{cut}})}{\partial r^{\alpha\beta}}\right). \qquad (56)\end{aligned}$$

The last term containing the weak derivative of the Dirac delta function can be simplified through various identities (see Appendix B) to obtain the following equation:

$$\frac{\partial^2 U_{\mathrm{HScut}}}{\partial r^{\alpha\beta 2}} = \frac{\partial^2 U}{\partial r^{\alpha\beta 2}} - \frac{\partial^2 U}{\partial r^{\alpha\beta 2}} H(r^{\alpha\beta} - r_{\mathrm{cut}}) - \frac{\partial U}{\partial r^{\alpha\beta}}\delta(r^{\alpha\beta} - r_{\mathrm{cut}}). \qquad (57)$$

The last term in Eq. (57) with the Dirac delta function is known as the impulsive correction to the second derivative of the potential.[5] In practice, impulsive corrections to the first and second derivatives are computed by replacing the delta function numerically by a simple normalized step function with a value of $\frac{1}{2w_{\mathrm{ic}}}$ for values of $r^{\alpha\beta}$ between $r_{\mathrm{cut}} - w_{\mathrm{ic}}$ and $r_{\mathrm{cut}} + w_{\mathrm{ic}}$ and zero otherwise, where w_{ic} is a small width relative to the particle radii.

To characterize the extent to which the impulsive correction affects the observed elastic properties, we simulated the solid and liquid argon systems using a potential that is truncated and shifted to zero at a cutoff of 1.1 nm. Figure 3 shows the values of c_{11} (with the Born term shown separately) and $\tilde{B}$ for a range of impulse widths from 1×10^{-5} to 0.01 nm. Starting with the Born term, c_{11}^{0}, in the solid system [Fig. 3(a)], it is clear that the impulsive correction makes a contribution far larger than the variation between runs despite being only ∼1% of the total value. The value of c_{11}^{0} shows minimal change for $w_{\mathrm{ic}} < 1 \times 10^{-4}$ nm, suggesting that this could be an optimal numerical threshold for the impulse width. While the fluctuation term introduces larger variations in the elastic coefficient c_{11} [Fig. 3(b)] and bulk modulus [Fig. 3(c)], the values obtained at different w_{ic} show that the impulsive correction is essential to accurately capture the elastic properties of the material. The value of the explicit deformation bulk modulus [$\tilde{B}^{\mathrm{ED}}$, red dotted-dashed line in Fig. 3(c)] is in excellent agreement with the impulsive corrected values of $\tilde{B}$.

In the case of liquid argon, we see that the impulsive correction induces a similar change to the Born term [Fig. 3(d)], yet the effect on the value of the full elastic coefficient c_{11} [Fig. 3(e)] is much larger in this case, as the impulse corrected values are 8%–9% smaller compared to the uncorrected c_{11}. Similarly, the uncorrected values of the bulk modulus are 5% larger than those with the impulse correction, which are also in excellent agreement with the bulk modulus obtained from the explicit deformation method [Fig. 3(f)]. In

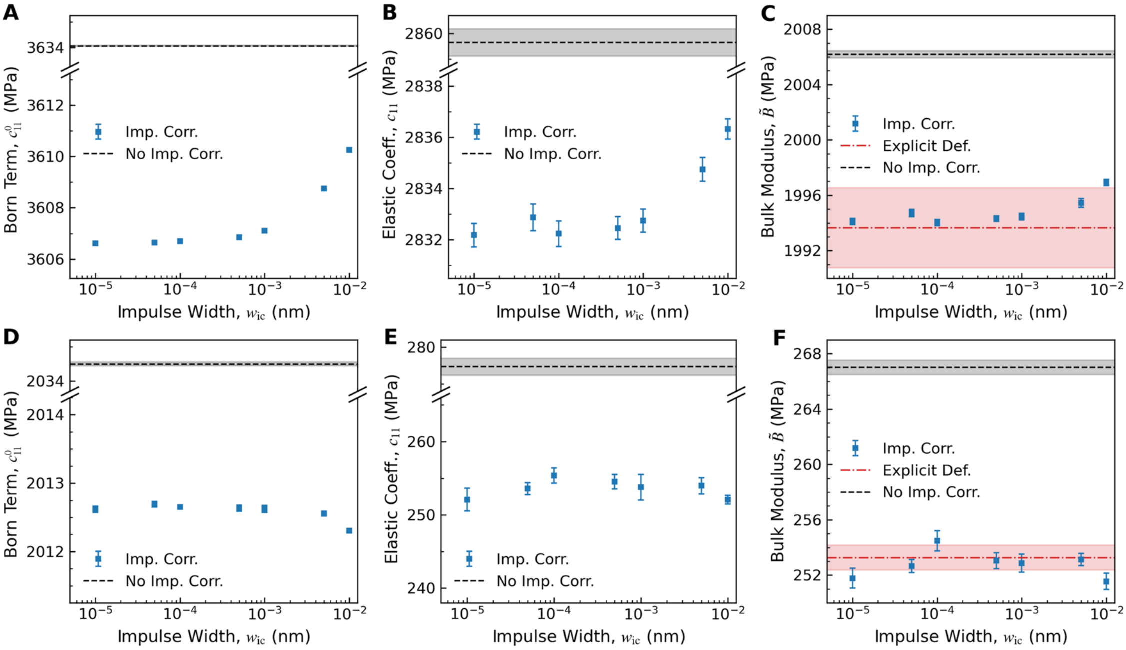

FIG. 3. Contribution of the impulsive correction to the elastic properties of solid and liquid argon simulated with a truncated and shifted potential (r_{cut} = 1.1 nm). Data for solid argon are shown in (a)–(c), while data for liquid argon are shown in (d)–(f). Panels show the Born term c_{11}^{0} [(a) and (d)], elastic coefficient c_{11} [(b) and (e)], and bulk modulus [(c) and (f)]. Values, including the impulsive correction, are shown as blue squares. Black dashed lines show the values without the impulsive correction, and red dotted-dashed lines show the values of the bulk modulus obtained from the explicit deformation method ($\tilde{B}^{\mathrm{ED}}$). Five independent simulations with different initial conditions were run and analyzed to obtain values at each impulse width. Shaded regions in lighter colors show the standard deviations of the corresponding quantities.

addition to this, the value of the uncorrected stress–strain shear modulus, $\tilde{c}_{44} = 7.25 \pm 0.04$ MPa, is inconsistent with the liquid nature of the material, despite having a relatively small magnitude. On the other hand, the impulse corrected stress–strain shear modulus has an average value of -0.02 ± 0.4 MPa, which is within the margin of error of the expected value of zero.

D. Coarse-grained molecular liquids

Having demonstrated the efficacy of the SSF method with the various argon systems, we now shift our focus to molecular liquids using the coarse-grained (CG) MARTINI 3.0 force-field. MARTINI has been widely used to model biomolecules and other soft materials, including lipids, proteins, and polymers, among many others.[53,75–78] We characterize four different CG MARTINI liquids, including water (1-bead), butane (1-bead), octane (2-beads), and dodecane (3-beads). These systems serve as a starting point to establish the effectiveness of the SSF method for future studies to determine the elastic properties of complex biological systems, such as lipid membranes. The 12-carbon dodecane molecule is the most complex of the four MARTINI systems tested. Dodecane is parameterized as 3 hydrophobic CG beads (see inset in Fig. 4) with the molecule's geometry determined by harmonic bonds (2-body) and angle (3-body) potentials. All four CG MARTINI liquids are simulated at a temperature of 310 K for compatibility with biomolecular systems and a pressure of 0.1 MPa (1 atm), except for butane, for which the pressure is set to 20 MPa due to its lower boiling point.

Given the coarse-grained nature of MARTINI as well as the molecular nature of the liquids, we first evaluate the convergence of the SSF method for dodecane. Analysis of the autocorrelation times of the pressure tensor (Fig. S5, computed from the ACFs of a short 8 ns *NVT* simulation) produced values of $\tau_{ii} = 0.32$ ps and $\tau_{ii} = 0.22$ ps, which are very similar to the values obtained for the atomistic argon systems. Figure S6 shows the convergence of c_{11}, c_{12}, and c_{44} for dodecane using sampling intervals of 0.2, 1.0, and 2.0 ps with three independent simulation runs of 2500 ns for each interval. The pattern of convergence for dodecane shows very similar trends to those observed for the atomistic argon systems, although convergence in the CG molecular fluid requires a larger number of samples ($\sim 1 \times 10^6$) at the longest sampling interval. The average final values of the elastic coefficients for dodecane are within error of each other (see Table S3), regardless of the sampling interval, as long as a sufficient number of simulation frames are analyzed.

As MARTINI is parameterized using a Lennard-Jones potential with a truncated and shifted potential at a 1.1 nm cutoff, we also examine the effect of the impulsive correction on the elastic properties of dodecane, as shown in Fig. 4. Similarly to the liquid

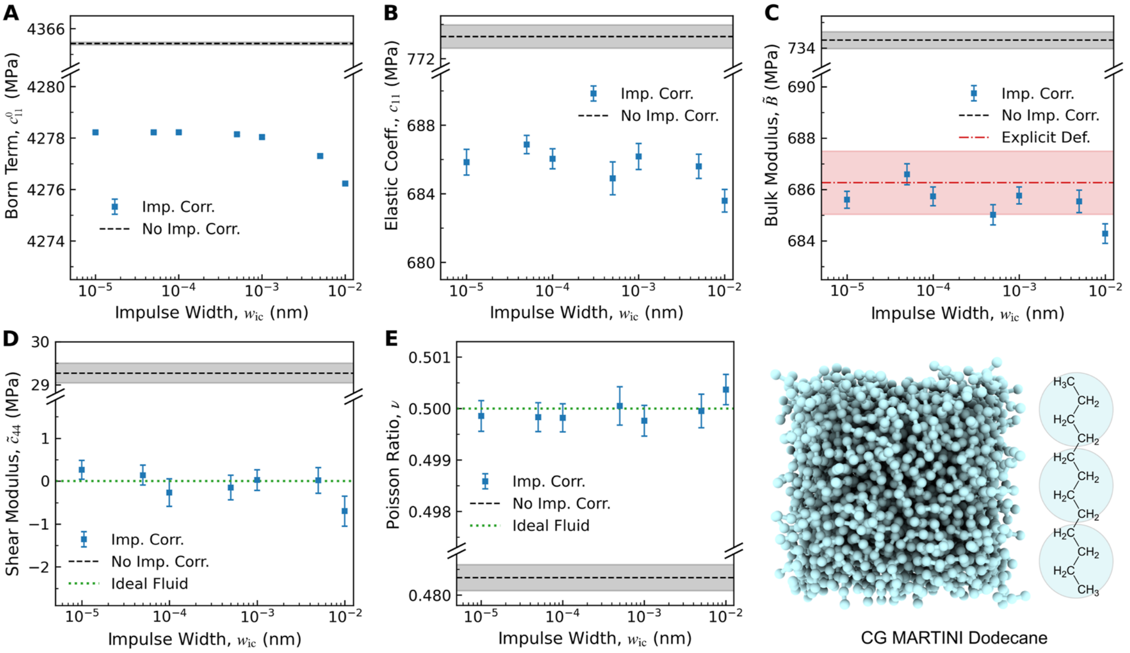

FIG. 4. Contribution of the impulsive correction to the elastic properties of CG MARTINI 3.0 liquid dodecane simulated with a truncated and shifted potential ($r_{\text{cut}} = 1.1$ nm). Panels show the Born term c^0_{11} (a), elastic coefficient c_{11} (b), bulk modulus (c), stress–strain shear modulus $\tilde{c}_{44}$ (d), and the Poisson ratio (e). Values, including the impulsive correction, are shown as blue squares. Black dashed lines show the values without the impulsive correction, dotted green lines show the expected values for an ideal fluid, and red dotted-dashed lines show the values of the bulk modulus obtained from the explicit deformation method ($\tilde{B}^{\text{ED}}$). Five independent simulations with different initial conditions were run and analyzed to obtain values at each impulse width. Shaded regions in lighter colors show the standard deviations of the corresponding quantities. The inset on the bottom right shows a snapshot of a CG MARTINI dodecane simulation and the mapping between the 12-carbon atomistic molecule and the 3-bead CG representation.

argon system, the impulsive correction reduces the value of the Born term by ~2%, which levels off for impulse widths $w_{\mathrm{ic}} < 1 \times 10^{-4}$ [Fig. 4(a)]. The effect of the impulsive correction on c_{11} [Fig. 4(b)] and the bulk modulus [Fig. 4(c)] is much more drastic, with the value changing by almost 11% and 7%, respectively. The impulse corrected values of $\tilde{B}$ are in excellent agreement with the result from the explicit deformation method ($\tilde{B}^{\mathrm{ED}}$). The impulse correction is also essential in obtaining the expected behavior for a liquid, as the values of the stress–strain shear modulus [Fig. 4(d)] hover near zero while the uncorrected value of $\tilde{c}_{44} = 29.3 \pm 0.2$ has a considerable magnitude. Similarly, the impulse corrected values of the Poisson ratio are in excellent agreement with the expected value of 0.5 for an ideal fluid [Fig. 4(e)].

The elastic properties of all four MARTINI liquids are shown in Table III. In general terms, the elastic coefficients c_{11} and c_{12}, as well as the bulk modulus, increase with magnitude as the hydrocarbon chain length grows (butane < octane < dodecane), as expected from the larger number of intermolecular interactions. Although water has a smaller mass than butane, the CG MARTINI single-bead water has larger elastic coefficients and bulk modulus compared to the other three hydrophobic molecules, which is a result of the model's parameterization to reproduce experimental observations such as the high surface tension and melting point of water. While the opposing Born and fluctuation terms have significantly different values for c_{11}, c_{12}, and c_{44} across all the liquids, the resulting elastic coefficients maintain the relation $c_{44} = \frac{1}{2}(c_{11} - c_{12})$ as expected for isotropic materials (Table III). This is remarkablec given the generally much larger magnitude of the Born and fluctuation terms compared to their corresponding elastic coefficients. In addition, note that the Born term for the c_{12} and c_{44} coefficients is identical by construction for the three liquids that only have 2-body potentials (butane, octane, and water). However, in the case of dodecane, the 3-body angle potential introduces an asymmetry in the values of the Born term for c_{12} and c_{44}. As expected for ideal fluids, the values of the stress–strain shear modulus, $\tilde{c}_{44}$, are near zero, and the values of the Poisson ratio are near 0.5 for all four CG MARTINI liquids. The values of the bulk modulus, $\tilde{B}$, obtained from the SSF method are also in excellent agreement with the values obtained from the explicit deformation ($\tilde{B}^{\mathrm{ED}}$) and volume fluctuation ($\tilde{B}^{\mathrm{VF}}$) methods for all the liquids tested.

Before concluding this section, we make a note regarding numerical simulation choices that may have significant effects on the observed elastic properties of CG systems in particular. Increasing the simulation time step can have negative effects on the observed values of the elastic coefficients, as shown in Table S4. For example, when simulating water at the default MARTINI time step of 0.02 ps, the elastic coefficient c_{11} has a slightly lower value than c_{12}, and c_{44} is negative beyond the error in the measurements. Increasing the time step to 0.04 ps increases this discrepancy even further, indicating that the time step is the source of the problem. We find that a time step of 0.005 ps is the safest choice for the MARTINI force-field to obtain consistent elastic coefficients. While the Newtonian mechanics may be stable for large time steps in the CG force-field, the underlying Hamiltonian dynamics may not be

TABLE III. Elastic properties of CG MARTINI 3.0 liquids with 2- and 3-body bonded potentials.

	Butane	Octane	Dodecane	Water
P (MPa)	1.99 ± 0.02	0.12 ± 0.03	0.10 ± 0.03	0.10 ± 0.02
T (K)	309.97 ± 0.03	309.97 ± 0.02	309.98 ± 0.02	309.97 ± 0.03
c_{11} ($\tilde{c}_{11}$) (MPa)[a]	272.7 ± 0.4 (270.7)	571.6 ± 0.7 (571.6)	685.8 ± 0.7 (685.8)	917.3 ± 0.7 (917.3)
Born	2397.66 ± 0.02	3819.17 ± 0.03	4278.22 ± 0.05	4715.05 ± 0.03
Fluct.	-2246.9 ± 0.4	-3385.6 ± 0.7	-3734.2 ± 0.8	-3937.6 ± 0.7
Kin.	121.886 ± 0.001	138.028 ± 0.001	141.786 ± 0.001	139.853 ± 0.001
c_{12} ($\tilde{c}_{12}$) (MPa)	268.9 ± 0.3 (270.8)	571.2 ± 0.5 (571.2)	685.5 ± 0.4 (685.5)	916.2 ± 0.5 (916.3)
Born	799.21 ± 0.04	1273.06 ± 0.04	1416.94 ± 0.05	1571.65 ± 0.06
Fluct.	-533.3 ± 0.2	-701.9 ± 0.4	-731.5 ± 0.3	-655.4 ± 0.5
Kin.	0.0 ± 0.0	0.0 ± 0.0	0.0 ± 0.0	0.0 ± 0.0
c_{44} ($\tilde{c}_{44}$) (MPa)	1.9 ± 0.2 (0.0)	0.0 ± 0.3 (0.0)	0.32 ± 0.22 (0.26)	-0.42 ± 0.31 (-0.47)
Born	799.21 ± 0.04	1273.06 ± 0.04	1430.64 ± 0.05	1571.65 ± 0.06
Fluct.	-858.3 ± 0.2	-1342.1 ± 0.2	-1501.2 ± 0.2	-1642.0 ± 0.3
Kin.	60.943 ± 0.001	69.014 ± 0.001	70.893 ± 0.001	69.926 ± 0.001
ν[b]	0.5001 ± 0.0004	0.4998 ± 0.0004	0.4999 ± 0.0003	0.4997 ± 0.0003
$\tilde{B}$ (MPa)[c]	270.8 ± 0.2	571.3 ± 0.4	685.6 ± 0.4	916.6 ± 0.4
$\tilde{B}^{\mathrm{ED}}$ (MPa)[d]	271.0 ± 0.9	571 ± 2	686 ± 2	914 ± 2
$\tilde{B}^{\mathrm{VF}}$ (MPa)[e]	273 ± 1	569 ± 4	688 ± 5	914 ± 9

[a] Data inside the box are computed through the SSF method [Eq. (30)].

[b] Obtained from Eq. (47).

[c] Obtained from Eq. (46).

[d] Computed through the explicit deformation method using Eq. (48).

[e] Computed through the volume fluctuation method using Eq. (49).

properly integrated, which may affect the conservation of energy and its associated energy fluctuations, as has been previously discussed by Winger *et al.*[79]

V. CONCLUSIONS

We have demonstrated through numerous systems that the SSF method is a very effective tool in estimating the elastic coefficients of materials from MD simulations. We have shown that the SSF method produces elastic moduli for materials in the solid, liquid, and gas phases in excellent agreement with other approaches, such as the explicit deformation and volume fluctuation methods, despite earlier reports that suggested the SSF formula was not suitable to analyze the elastic properties of fluid-like materials.[49–51] Obtaining accurate and physically meaningful results for liquid systems requires increased sampling as well as proper inclusion of the impulsive correction term for long-range potentials such as Lennard-Jones that are truncated at a cutoff radius. Without the impulsive correction, the shear modulus, $\tilde{c}_{44}$, for the liquid systems would have unphysical non-zero values, and the Poisson ratio would significantly deviate from the expected value of 0.5 for an ideal fluid. Furthermore, we have shown that the negative fluctuation term significantly softens the elastic response of fluid materials, as it has a similar magnitude compared to the Born term. The elastic characterization of molecular fluids using the MARTINI CG force-field, which includes multi-body potentials, shows that the SSF coefficients and moduli are in remarkably close agreement with other methods. However, accurate characterization of CG models with the SSF method requires a careful choice of simulation parameters, including a significant decrease in the step size from the commonly used default value of 0.02 ps to the better suited timestep of 0.005 ps. Our extensive validation of bulk soft materials provides a solid foundation to apply the SSF method to study the local elastic properties of non-homogeneous biomolecular systems, such as lipid membranes, in our companion paper.[54]

SUPPLEMENTARY MATERIAL

See the supplementary material for additional figures, including autocorrelation functions of the pressure tensor, convergence of the elastic coefficients, and explicit deformation of argon systems, as well as additional tables, including values of the elastic coefficients computed at different sampling intervals and different integration time steps. The supplementary material also contains definitions of all the bonded and non-bonded interatomic potentials used in this study, including their first and second derivatives.

ACKNOWLEDGMENTS

J.M.V. and A.L.L. acknowledge the support of the National Science Foundation through Grant No. CHE-1944892/2326678. Computations were performed, in part, on the Vermont Advanced Computing Core, supported in part by NSF Award No. OAC-1827314. This work also used the NCSA Delta supercomputer at the University of Illinois at Urbana-Champaign through allocation BIO240313 from the Advanced Cyberinfrastructure Coordination Ecosystem: Services and Support (ACCESS) program, which is supported by U.S. National Science Foundation Grant Nos. 2138259, 2138286, 2138307, 2137603, and 2138296.

AUTHOR DECLARATIONS

Conflict of Interest

The authors have no conflicts to disclose.

Author Contributions

Andrew L. Lewis: Conceptualization (equal); Data curation (equal); Formal analysis (equal); Methodology (equal); Software (equal); Validation (equal); Visualization (equal); Writing – original draft (equal); Writing – review & editing (equal). **Benjamin Himberg**: Conceptualization (equal); Investigation (equal); Methodology (equal); Software (equal). **Alejandro Torres-Sánchez**: Conceptualization (equal); Formal analysis (equal); Methodology (equal); Software (equal); Writing – review & editing (equal). **Juan M. Vanegas**: Conceptualization (lead); Data curation (equal); Formal analysis (equal); Funding acquisition (lead); Investigation (equal); Methodology (equal); Resources (equal); Software (equal); Supervision (equal); Validation (equal); Visualization (equal); Writing – original draft (lead); Writing – review & editing (equal).

DATA AVAILABILITY

The data that support the findings of this study are available from the corresponding author upon reasonable request. The custom GROMACS-LS and MDStress library codes are available from the project website at https://github.com/vanegasj/gromacs-ls and have also been deposited in the Zenodo repository.[61]

APPENDIX A: DEFORMATION GRADIENT IDENTITIES

This section contains definitions, identities, and manipulations used when deriving the SSF formula using the method of dilatation. As mentioned in the main text, the deformation gradient can be defined as

$$F_{i,J} = \frac{\partial r_i}{\partial R_J}, \tag{A1}$$

where r_i and R_J are the positions in the deformed and reference configurations, respectively. In 3-dimensions, the deformation gradient takes the following matrix form:

$$\boldsymbol{F} = \begin{bmatrix} \frac{\partial r_1}{\partial R_1} & \frac{\partial r_1}{\partial R_2} & \frac{\partial r_1}{\partial R_3} \\ \frac{\partial r_2}{\partial R_1} & \frac{\partial r_2}{\partial R_2} & \frac{\partial r_2}{\partial R_3} \\ \frac{\partial r_3}{\partial R_1} & \frac{\partial r_3}{\partial R_2} & \frac{\partial r_3}{\partial R_3} \end{bmatrix}. \tag{A2}$$

Similarly, one can define the inverse of the deformation or pull-back gradient as

$$F^{-1}_{I,j} = \frac{\partial R_I}{\partial r_j}. \tag{A3}$$

The pull-back gradient is a mapping that takes the deformed configuration back to the reference configuration. The deformation and pull-back gradient tensors are two-point tensors, which are generally not symmetric. However, they satisfy the following identities:

$$\begin{aligned} F_{i,K}F^{-1}_{K,j} &= \delta_{ij}, \\ F^{-1}_{I,k}F_{k,J} &= \delta_{IJ}, \end{aligned} \tag{A4}$$

$$F^{T}_{i,J} = F_{j,I}, \tag{A5}$$

$$F^{-T}_{I,j} = F^{-1}_{J,i}, \tag{A6}$$

$$\frac{\partial F_{i,J}}{\partial F_{k,L}} = \delta_{ik}\delta_{JL}, \tag{A7}$$

$$\frac{\partial F^{-1}_{J,i}}{\partial F_{k,L}} = -F^{-1}_{J,k}F^{-1}_{L,i}. \tag{A8}$$

Under a canonical transformation, the positions of particle α in the deformed and reference configurations are mapped by

$$r^{\alpha}_{i} = F_{i,J}R^{\alpha}_{J}, \tag{A9}$$

$$R^{\alpha}_{I} = F^{-1}_{I,j}r^{\alpha}_{j}. \tag{A10}$$

Similarly, the momentum of particle α in the deformed configuration is mapped to the conjugate momentum in the reference configuration by

$$p^{\alpha}_{i} = F^{-1}_{J,i}P^{\alpha}_{J}, \tag{A11}$$

$$P^{\alpha}_{I} = F_{j,I}p^{\alpha}_{j}. \tag{A12}$$

From these relations, we can define the first and second derivatives of the deformed positions and momenta as

$$\frac{\partial r^{\alpha}_{q}}{\partial F_{i,J}} = R^{\alpha}_{J}\delta_{qi}, \tag{A13}$$

$$\frac{\partial^2 r^{\alpha}_{q}}{\partial F_{i,J}\partial F_{k,L}} = 0, \tag{A14}$$

$$\frac{\partial p^{\alpha}_{q}}{\partial F_{i,J}} = -F^{-1}_{J,q}p^{\alpha}_{i}, \tag{A15}$$

$$\frac{\partial^2 p^{\alpha}_{q}}{\partial F_{i,J}\partial F_{k,L}} = F^{-1}_{L,i}F^{-1}_{J,q}p^{\alpha}_{k} + F^{-1}_{J,k}F^{-1}_{L,q}p^{\alpha}_{i}. \tag{A16}$$

We include two additional identities related to the determinant of the deformation gradient, $\det(\boldsymbol{F})$. The determinant of the deformation gradient is often used to describe the ratio of the volume of the deformed configuration to the volume of the reference configuration,

$$\det(\boldsymbol{F}) = \frac{1}{3!}\varepsilon_{ijk}\varepsilon_{LMN}F_{i,L}F_{j,M}F_{k,N} = \frac{V}{V_0}, \tag{A17}$$

where ε is the Levi–Cività symbol. The derivative

$$\frac{\partial \det(\boldsymbol{F})}{\partial F_{i,J}} = \operatorname{adj}(\boldsymbol{F}) = \det(\boldsymbol{F})F^{-1}_{J,i} \tag{A18}$$

is required to define Nanson's relation and the mixed elasticity tensor.

APPENDIX B: DERIVATIVES OF GENERALIZED FUNCTIONS

Generalized function theory, or distribution theory, gives a framework for defining operations for functions and distributions with discontinuities such as the Heaviside step function and the Dirac delta function (see Lighthill[80]). One possible piecewise representation of the Heaviside step function is

$$H(x - x_0) = \begin{cases} 0, & x < x_0, \\ 1, & x \geq x_0, \end{cases} \tag{B1}$$

and the Dirac delta function is often represented as the following piecewise function:

$$\delta(x - x_0) = \begin{cases} 0, & x \neq x_0, \\ \infty, & x = x_0. \end{cases} \tag{B2}$$

These two functions can also be represented as Fourier integrals in the form of

$$H(x - x_0) = \lim_{\epsilon \to 0^+} \frac{1}{2\pi i}\int_{-\infty}^{\infty} \frac{1}{k - i\epsilon} e^{ik(x - x_0)}\, dk \tag{B3}$$

and

$$\delta(x - x_0) = \frac{1}{2\pi}\int_{-\infty}^{\infty} e^{ik(x - x_0)}\, dk. \tag{B4}$$

One can assert by inspection of the above equations that the Dirac delta function is the derivative of the Heaviside step function,

$$\frac{dH(x - x_0)}{dx} = \delta(x - x_0). \tag{B5}$$

Rigorously defining this assertion requires an operation called the weak derivative, which defines the derivative for discontinuous functions and distributions. The weak derivative is an extension of the derivative to generalized functions. Suppose we have a generalized function or distribution, $f(x)$, and a "good" function, $\phi(x)$, as well as their respective derivatives $f'(x)$ and $\phi'(x)$. Informally, a "good" function is a function that is infinitely differentiable for every point inside its domain. Starting from integration by parts,

$$\int_a^b f'(x)\phi(x)dx = f(x)\phi(x)\Big|_a^b - \int_a^b f(x)\phi'(x)dx, \tag{B6}$$

an integral definition of the weak derivative can be obtained as

$$\int_a^b f(x)\phi'(x)dx = -\int_a^b f'(x)\phi(x)dx, \tag{B7}$$

where a and b are chosen such that $f(a)\phi(a) = f(b)\phi(b)$ for the set of all "good" functions. When two integrals over the same set of bounds are equivalent, then their integrands must be equivalent, and therefore the following relation must hold:

$$f'(x)\phi(x) = -f(x)\phi'(x). \tag{B8}$$

Generalizing this procedure to the nth order derivative gives

$$f^{(n)}(x)\phi(x) = (-1)^n f(x)\phi^{(n)}(x). \tag{B9}$$

When Eqs. (B3), (B4), and (B7) hold and are combined with an appropriate choice of "good" function, e.g., $\phi(x) = e^{-x^2}$, one can show Eq. (B5) is true. This can be generalized to show that the derivative of the Dirac delta function, $\delta(x - x_0)$, for some choice of "good" function, $\phi(x)$, is

$$\delta^{(n)}(x - x_0)\phi(x) = (-1)^n \delta(x - x_0)\phi^{(n)}(x). \tag{B10}$$

REFERENCES

[1] D. R. Squire, A. C. Holt, and W. G. Hoover, "Isothermal elastic constants for argon. Theory and Monte Carlo calculations," Physica **42**, 388–397 (1969).

[2] A. A. Gusev, M. M. Zehnder, and U. W. Suter, "Fluctuation formula for elastic constants," Phys. Rev. B **54**, 1–4 (1996).

[3] J. R. Ray, M. C. Moody, and A. Rahman, "Calculation of elastic constants using isothermal molecular dynamics," Phys. Rev. B **33**, 895–899 (1986).

[4] G. Clavier, N. Desbiens, E. Bourasseau, V. Lachet, N. Brusselle-Dupend, and B. Rousseau, "Computation of elastic constants of solids using molecular simulation: Comparison of constant volume and constant pressure ensemble methods," Mol. Simul. **43**, 1413–1422 (2017).

[5] H. Xu, J. P. Wittmer, P. Polińska, and J. Baschnagel, "Impulsive correction to the elastic moduli obtained using the stress-fluctuation formalism in systems with truncated pair potential," Phys. Rev. E **86**, 046705 (2012).

[6] J. P. Wittmer, H. Xu, P. Polińska, F. Weysser, and J. Baschnagel, "Shear modulus of simulated glass-forming model systems: Effects of boundary condition, temperature, and sampling time," J. Chem. Phys. **138**, 12A533 (2013).

[7] P. B. Canham, "The minimum energy of bending as a possible explanation of the biconcave shape of the human red blood cell," J. Theor. Biol. **26**, 61–81 (1970).

[8] W. Helfrich, "Elastic properties of lipid bilayers: Theory and possible experiments," Z. Naturforsch. C **28**, 693–703 (1973).

[9] W. Helfrich and M. M. Kozlov, "Bending tensions and the bending rigidity of fluid membranes," J. Phys. II Fr. **3**, 287–292 (1993).

[10] M. M. Terzi and M. Deserno, "Novel tilt-curvature coupling in lipid membranes," J. Chem. Phys. **147**, 084702 (2017).

[11] M. M. Terzi, M. F. Ergüder, and M. Deserno, "A consistent quadratic curvature-tilt theory for fluid lipid membranes," J. Chem. Phys. **151**, 164108 (2019).

[12] M. Hamm and M. M. Kozlov, "Elastic energy of tilt and bending of fluid membranes," Eur. Phys. J. E **3**, 323–335 (2000).

[13] F. Campelo, C. Arnarez, S. J. Marrink, and M. M. Kozlov, "Helfrich model of membrane bending: From Gibbs theory of liquid interfaces to membranes as thick anisotropic elastic layers," Adv. Colloid Interface Sci. **208**, 25–33 (2014).

[14] U. Seifert, K. Berndl, and R. Lipowsky, "Shape transformations of vesicles: Phase diagram for spontaneous- curvature and bilayer-coupling models," Phys. Rev. A **44**, 1182 (1991).

[15] X. Li, P. M. Vlahovska, and G. E. Karniadakis, "Continuum- and particle-based modeling of shapes and dynamics of red blood cells in health and disease," Soft Matter **9**, 28–37 (2013).

[16] P. Rangamani, A. Benjamini, A. Agrawal, B. Smit, D. J. Steigmann, and G. Oster, "Small scale membrane mechanics," Biomech. Model. Mechanobiol. **13**, 697–711 (2013).

[17] Y. Tang, J. Yoo, A. Yethiraj, Q. Cui, and X. Chen, "Mechanosensitive channels: Insights from continuum-based simulations," Cell Biochem. Biophys. **52**, 1–18 (2008).

[18] A. J. Sodt, A. H. Beaven, O. S. Andersen, W. Im, and R. W. Pastor, "Gramicidin A channel formation induces local lipid redistribution II: A 3D continuum elastic model," Biophys. J. **112**, 1198–1213 (2017).

[19] R. Dimova, "Recent developments in the field of bending rigidity measurements on membranes," Adv. Colloid Interface Sci. **208**, 225–234 (2014).

[20] M. F. Ergüder and M. Deserno, "Identifying systematic errors in a power spectral analysis of simulated lipid membranes," J. Chem. Phys. **154**, 214103 (2021).

[21] K. C. Sapp, A. H. Beaven, and A. J. Sodt, "Spatial extent of a single lipid's influence on bilayer mechanics," Phys. Rev. E **103**, 042413 (2021).

[22] M. Hu, J. J. Briguglio, and M. Deserno, "Determining the Gaussian curvature modulus of lipid membranes in simulations," Biophys. J. **102**, 1403–1410 (2012).

[23] X. Wang and M. Deserno, "Determining the lipid tilt modulus by simulating membrane buckles," J. Phys. Chem. B **120**, 6061–6073 (2016).

[24] J. F. Nagle, E. A. Evans, P. Bassereau, T. Baumgart, S. Tristram-Nagle, and R. Dimova, "A needless but interesting controversy," Proc. Natl. Acad. Sci. U. S. A. **118**, e2025011118 (2021).

[25] F. Heinrich and J. F. Nagle, "The effect of cholesterol on the bending modulus of DOPC bilayers: Re-analysis of NSE data," Soft Matter **21**, 2258–2267 (2025).

[26] R. Ashkar, M. Doktorova, F. a. Heberle, H. L. Scott, F. N. Barrera, J. Katsaras, G. Khelashvili, and M. F. Brown, "Reply to Nagle et al.: The universal stiffening effects of cholesterol on lipid membranes," Proc. Natl. Acad. Sci. U. S. A. **118**, e2102845118 (2021).

[27] E. G. Brandt, A. R. Braun, J. N. Sachs, J. F. Nagle, and O. Edholm, "Interpretation of fluctuation spectra in lipid bilayer simulations," Biophys. J. **100**, 2104–2111 (2011).

[28] J. F. Nagle, M. S. Jablin, S. Tristram-Nagle, and K. Akabori, "What are the true values of the bending modulus of simple lipid bilayers?," Chem. Phys. Lipids **185**, 3–10 (2015).

[29] J. F. Nagle, "Experimentally determined tilt and bending moduli of single-component lipid bilayers," Chem. Phys. Lipids **205**, 18–24 (2017).

[30] M. Parrinello and A. Rahman, "Strain fluctuations and elastic constants," J. Chem. Phys. **76**, 2662–2666 (1982).

[31] T. H. K. Barron and M. L. Klein, "Second-order elastic constants of a solid under stress," Proc. Phys. Soc. **85**, 523–532 (1965).

[32] F. Bavaud, P. Choquard, and J. R. Fontaine, "Statistical mechanics of elastic moduli," J. Stat. Phys. **42**, 621–646 (1986).

[33] J. F. Lutsko, "Stress and elastic constants in anisotropic solids: Molecular dynamics techniques," J. Appl. Phys. **64**, 1152–1154 (1988).

[34] J. F. Lutsko, "Generalized expressions for the calculation of elastic constants by computer simulation," J. Appl. Phys. **65**, 2991–2997 (1989).

[35] G. Clavier and A. P. Thompson, "Computation of the thermal elastic constants for arbitrary manybody potentials in LAMMPS using the stress-fluctuation formalism," Comput. Phys. Commun. **286**, 108674 (2023).

[36] Y. Zhen and C. Chu, "A deformation–fluctuation hybrid method for fast evaluation of elastic constants with many-body potentials," Comput. Phys. Commun. **183**, 261–265 (2012).

[37] M. Bernetti and G. Bussi, "Pressure control using stochastic cell rescaling," J. Chem. Phys. **153**, 114107 (2020).

[38] E. B. Tadmor and R. E. Miller, *Modeling Materials: Continuum, Atomistic, and Multiscale Techniques* (Cambridge University Press, Cambridge; New York, 2011).

[39] K. Yoshimoto, G. J. Papakonstantopoulos, J. F. Lutsko, and J. J. de Pablo, "Statistical calculation of elastic moduli for atomistic models," Phys. Rev. B **71**, 184108 (2005).

[40] M. Born and K. Huang, *Dynamical Theory of Crystal Lattices* (Oxford University Press, 1954).

[41] K. Huang, "On the atomic theory of elasticity," Proc. R. Soc. London, Ser. A **203**, 178–194 (1950).

[42] N. C. Admal and E. B. Tadmor, "A unified interpretation of stress in molecular systems," J. Elasticity **100**, 63–143 (2010).

[43] K. Van Workum, G. Gao, J. D. Schall, and J. A. Harrison, "Expressions for the stress and elasticity tensors for angle-dependent potentials," J. Chem. Phys. **125**, 144506 (2006).

[44] J. Grießer, L. Frérot, J. A. Oldenstaedt, M. H. Müser, and L. Pastewka, "Analytic elastic coefficients in molecular calculations: Finite strain, nonaffine displacements, and many-body interatomic potentials," Phys. Rev. Mater. **7**, 073603 (2023).

[45] J. M. Vanegas, A. Torres-Sánchez, and M. Arroyo, "Importance of force decomposition for local stress calculations in biomembrane molecular simulations," J. Chem. Theory Comput. **10**, 691–702 (2014).

[46] A. Torres-Sánchez, J. M. Vanegas, and M. Arroyo, "Examining the mechanical equilibrium of microscopic stresses in molecular simulations," Phys. Rev. Lett. **114**, 258102 (2015).

[47] A. Torres-Sánchez, J. M. Vanegas, and M. Arroyo, "Geometric derivation of the microscopic stress: A covariant central force decomposition," J. Mech. Phys. Solids **93**, 224–239 (2016).

[48] K. Van Workum, K. Yoshimoto, J. de Pablo, and J. Douglas, "Isothermal stress and elasticity tensors for ions and point dipoles using Ewald summations," Phys. Rev. E **71**, 061102 (2005).

[49] S. J. Barsky, M. Plischke, B. Joós, and Z. Zhou, "Elastic properties of randomly cross-linked polymers," Phys. Rev. E **54**, 5370–5376 (1996).

[50] Z. Zhou and B. Joós, "Convergence issues in molecular dynamics simulations of highly entropic materials," Modell. Simul. Mater. Sci. Eng. **7**, 383–395 (1999).

[51] Z. Zhou and B. Joós, "Stability criteria for homogeneously stressed materials and the calculation of elastic constants," Phys. Rev. B **54**, 3841–3850 (1996).

[52] D. Lips and P. Maass, "Stress-stress fluctuation formula for elastic constants in the *NPT* ensemble," Phys. Rev. E **97**, 053002 (2018).

[53] P. C. T. Souza, R. Alessandri, J. Barnoud, S. Thallmair, I. Faustino, F. Grünewald, I. Patmanidis, H. Abdizadeh, B. M. H. Bruininks, T. A. Wassenaar, P. C. Kroon, J. Melcr, V. Nieto, V. Corradi, H. M. Khan, J. Domański, M. Javanainen, H. Martinez-Seara, N. Reuter, R. B. Best, I. Vattulainen, L. Monticelli, X. Periole, D. P. Tieleman, A. H. de Vries, and S. J. Marrink, "Martini 3: A general purpose force field for coarse-grained molecular dynamics," Nat. Methods **18**, 382–388 (2021).

[54] A. L. Lewis, B. Himberg, A. Torres-Sánchez, and J. M. Vanegas, "Microscopic elasticity from MD. II. Liquid interfaces and lipid membranes," J. Chem. Phys. **164**, 014703 (2025).

[55] F. D. Murnaghan, "Finite deformations of an elastic solid," Am. J. Math. **59**, 235–260 (1937).

[56] D. C. Wallace, "Thermoelasticity of stressed materials and comparison of various elastic constants," Phys. Rev. **162**, 776–789 (1967).

[57] D. C. Wallace, *Thermodynamics of Crystals* (John Wiley & Sons, Inc., New York, 1972).

[58] F. Birch, "Finite elastic strain of cubic crystals," Phys. Rev. **71**, 809–824 (1947).

[59] N. H. Scott, "An area modulus of elasticity: Definition and properties," J. Elasticity **58**, 269–275 (2000).

[60] M. J. Abraham, T. Murtola, R. Schulz, S. Páll, J. C. Smith, B. Hess, and E. Lindahl, "GROMACS: High performance molecular simulations through multi-level parallelism from laptops to supercomputers," SoftwareX **1–2**, 19–25 (2015).

[61] J. M. Vanegas, B. Himberg, A. Lewis, and A. Torres-Sánchez (2025). "GROMACS-LS and MDStress library: Tools for local stress and elasticity calculations," Zenodo. https://zenodo.org/records/17179200

[62] G. K. Horton and J. W. Leech, "On the statistical mechanics of the ideal inert gas solids," Proc. Phys. Soc. **82**, 816–854 (1963).

[63] G. Bussi, D. Donadio, and M. Parrinello, "Canonical sampling through velocity rescaling," J. Chem. Phys. **126**, 014101 (2007).

[64] H. Kim, B. Fábián, and G. Hummer, "Neighbor list artifacts in molecular dynamics simulations," J. Chem. Theory Comput. **19**, 8919–8929 (2023).

[65] C. R. Harris, K. J. Millman, S. J. van der Walt, R. Gommers, P. Virtanen, D. Cournapeau, E. Wieser, J. Taylor, S. Berg, N. J. Smith, R. Kern, M. Picus, S. Hoyer, M. H. van Kerkwijk, M. Brett, A. Haldane, J. F. del Río, M. Wiebe, P. Peterson, P. Gérard-Marchant, K. Sheppard, T. Reddy, W. Weckesser, H. Abbasi, C. Gohlke, and T. E. Oliphant, "Array programming with NumPy," Nature **585**, 357–362 (2020).

[66] P. Virtanen, R. Gommers, T. E. Oliphant, M. Haberland, T. Reddy, D. Cournapeau, E. Burovski, P. Peterson, W. Weckesser, J. Bright, S. J. van der Walt, M. Brett, J. Wilson, K. J. Millman, N. Mayorov, A. R. J. Nelson, E. Jones, R. Kern, E. Larson, C. J. Carey, İ. Polat, Y. Feng, E. W. Moore, J. VanderPlas, D. Laxalde, J. Perktold, R. Cimrman, I. Henriksen, E. A. Quintero, C. R. Harris, A. M. Archibald, A. H. Ribeiro, F. Pedregosa, P. van Mulbregt, and SciPy 1.0 Contributors, "SciPy 1.0: Fundamental algorithms for scientific computing in Python," Nat. Methods **17**, 261–272 (2020).

[67] J. D. Hunter, "Matplotlib: A 2D graphics environment," Comput. Sci. Eng. **9**, 90–95 (2007).

[68] H. Meixner, P. Leiderer, and E. Lüscher, "Temperature dependence of the hypersonic velocity in a single crystal of argon," Phys. Lett. A **37**, 39–40 (1971).

[69] H. Meixner, P. Leiderer, P. Berberich, and E. Lüscher, "The elastic constants of solid argon determined by stimulated Brillouin scattering," Phys. Lett. A **40**, 257–258 (1972).

[70] O. G. Peterson, D. N. Batchelder, and R. O. Simmons, "Measurements of X-ray lattice constant, thermal expansivity, and isothermal compressibility of argon crystals," Phys. Rev. **150**, 703–711 (1966).

[71] A. I. Epishin and D. S. Lisovenko, "Comparison of isothermal and adiabatic elasticity characteristics of the single crystal nickel-based superalloy CMSX-4 in the temperature range between room temperature and 1300°C," Mech. Solids **58**, 1587–1598 (2023).

[72] W. G. Hoover, A. C. Holt, and D. R. Squire, "Adiabatic elastic constants for argon. Theory and Monte Carlo calculations," Physica **44**, 437–443 (1969).

[73] W. Götze and H. Schmidt, "On three body forces in solid argon," Z. Phys. A Hadron Nucl. **192**, 409–418 (1966).

[74] G. N. Greaves, A. L. Greer, R. S. Lakes, and T. Rouxel, "Poisson's ratio and modern materials," Nat. Mater. **10**, 823–837 (2011).

[75] E. Panizon, D. Bochicchio, L. Monticelli, and G. Rossi, "MARTINI coarse-grained models of polyethylene and polypropylene," J. Phys. Chem. B **119**, 8209–8216 (2015).

[76] G. Rossi, P. F. J. Fuchs, J. Barnoud, and L. Monticelli, "A coarse-grained MARTINI model of polyethylene glycol and of polyoxyethylene alkyl ether surfactants," J. Phys. Chem. B **116**, 14353–14362 (2012).

[77] L. Borges-Araújo, I. Patmanidis, A. P. Singh, L. H. S. Santos, A. K. Sieradzan, S. Vanni, C. Czaplewski, S. Pantano, W. Shinoda, L. Monticelli, A. Liwo, S. J. Marrink, and P. C. T. Souza, "Pragmatic coarse-graining of proteins: Models and applications," J. Chem. Theory Comput. **19**, 7112–7135 (2023).

[78] S. J. Marrink, H. J. Risselada, S. Yefimov, D. P. Tieleman, and A. H. de Vries, "The MARTINI force field: Coarse grained model for biomolecular simulations," J. Phys. Chem. B **111**, 7812–7824 (2007).

[79] M. Winger, D. Trzesniak, R. Baron, and W. F. van Gunsteren, "On using a too large integration time step in molecular dynamics simulations of coarse-grained molecular models," Phys. Chem. Chem. Phys. **11**, 1934–1941 (2009).

[80] M. J. Lighthill, *An Introduction to Fourier Analysis and Generalised Functions*, *Cambridge Monographs on Mechanics* (Cambridge University Press, 1958).

SUPPLEMENTARY MATERIAL
Microscopic elasticity from MD part I: Bulk solid and fluid systems

Andrew L. Lewis
Department of Physics, The University of Vermont, Burlington, VT, USA.

Benjamin Himberg
Materials Science Graduate Program, The University of Vermont, Burlington, VT, USA.

Alejandro Torres-Sánchez
European Molecular Biology Laboratory, Barcelona, Spain.

Juan M. Vanegas*
Department of Biochemistry and Biophysics, Oregon State University, Corvallis, OR, USA.

(Dated: November 29, 2025)

---

* vanegasj@oregonstate.edu

I. SUPPLEMENTARY FIGURES

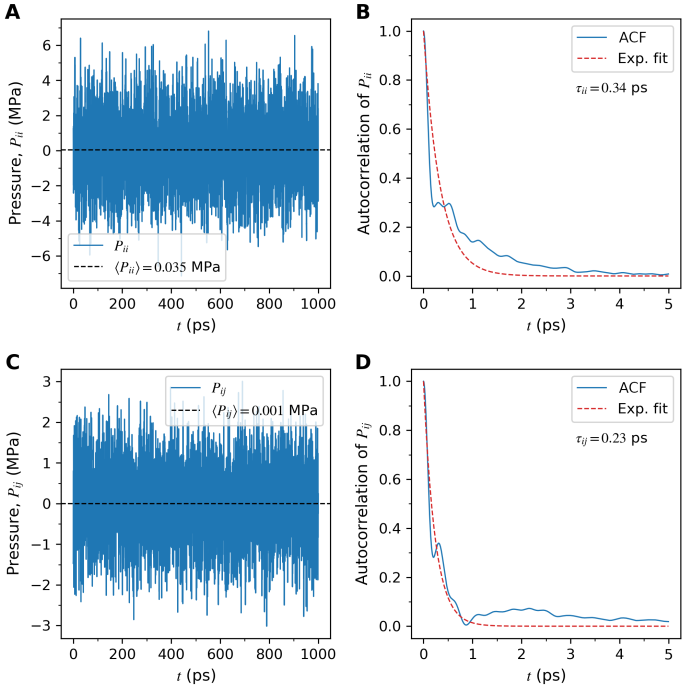

FIG. S1. Values of the diagonal, P_{ii}, and off-diagonal, P_{ij}, elements of the pressure tensor as a function of time and their autocorrelation function, $\mathrm{ACF}(t) = \langle f(t_0) f(t_0 + t)\rangle_{t_0}$, obtained from an equilibrated NVT simulation for solid argon. The autocorrelation functions were fitted to the simple exponential $\mathrm{ACF}(t) = \exp(-t/\tau)$ to obtain the average autocorrelation time, τ.

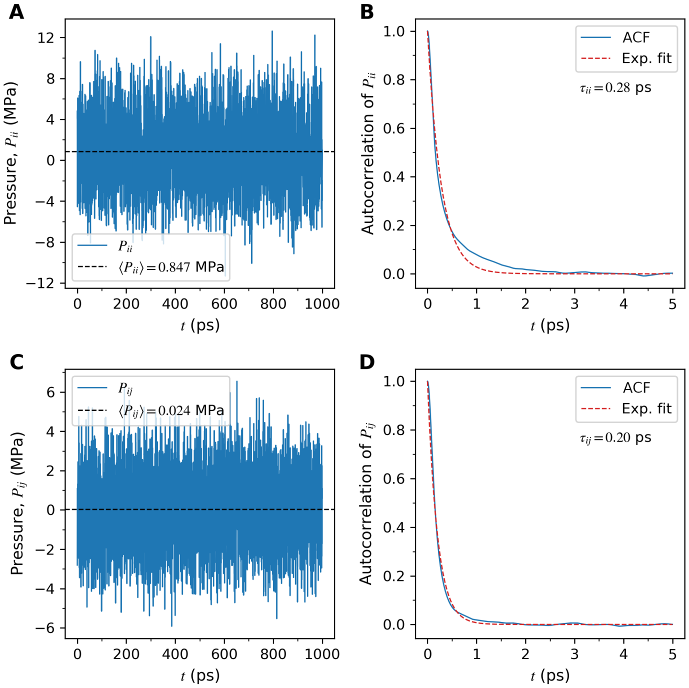

FIG. S2. Values of the diagonal, P_{ii}, and off-diagonal, P_{ij}, elements of the pressure tensor as a function of time and their autocorrelation function, $\mathrm{ACF}(t) = \langle f(t_0) f(t_0 + t)\rangle_{t_0}$, obtained from an equilibrated NVT simulation for liquid argon. The autocorrelation functions were fitted to the simple exponential $\mathrm{ACF}(t) = \exp(-t/\tau)$ to obtain the average autocorrelation time, τ.

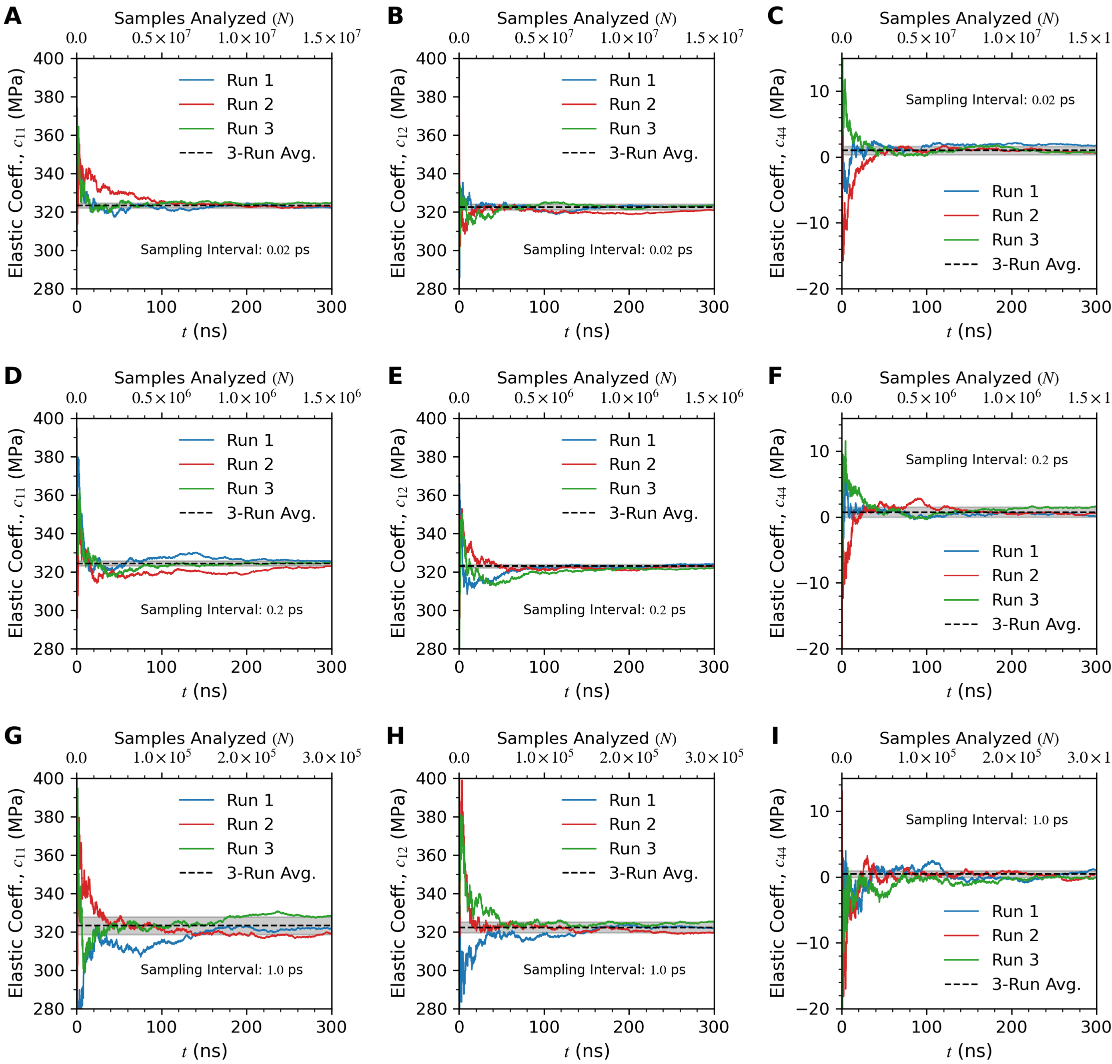

FIG. S3. Convergence of elastic coefficients for liquid argon using different sampling intervals. Top row (A-C) uses a sampling interval of 0.02 ps, middle row (D-F) 0.2 ps, and bottom row (G-I) 1.0 ps. Left panels show c_{11}, middle panels show c_{12}, and right panels show c_{44}. Three independent NVT simulations with different initial conditions were run at each sampling interval shown in blue, red, and green. Dashed black line shows the 3-run average value at the end of the simulations, while the gray shaded region shows the standard deviation.

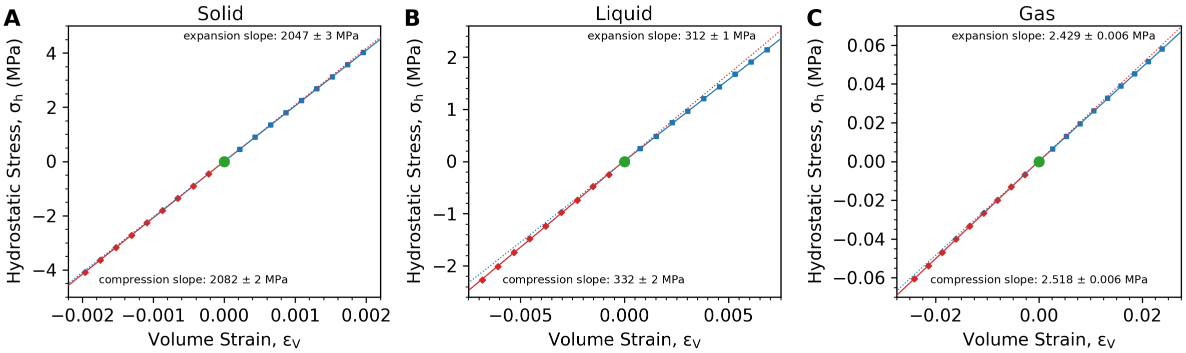

FIG. S4. Hydrostatic stress, $\sigma_h = \frac{1}{3}\mathrm{tr}(\boldsymbol{\sigma})$, as a function of the volume strain, $\varepsilon_V = \mathrm{tr}(\boldsymbol{\varepsilon})$, for simulations of argon in the solid (A), liquid (B), and gas (C) phases. The explicit deformation bulk modulus, $\tilde{B}^{\mathrm{ED}}$, is obtained from the average of the compression and expansion slopes.

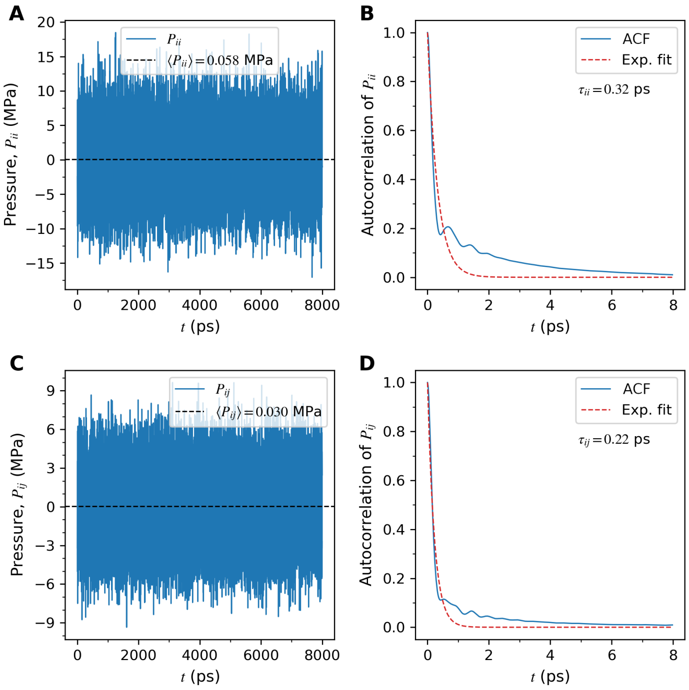

FIG. S5. Values of the diagonal, P_{ii}, and off-diagonal, P_{ij}, elements of the pressure tensor as a function of time and their autocorrelation function, $\mathrm{ACF}(t) = \langle f(t_0)f(t_0+t)\rangle_{t_0}$, obtained from an equilibrated NVT simulation for liquid dodecane (CG MARTINI). The autocorrelation functions were fitted to the simple exponential $\mathrm{ACF}(t) = \exp(-t/\tau)$ to obtain the average autocorrelation time, τ.

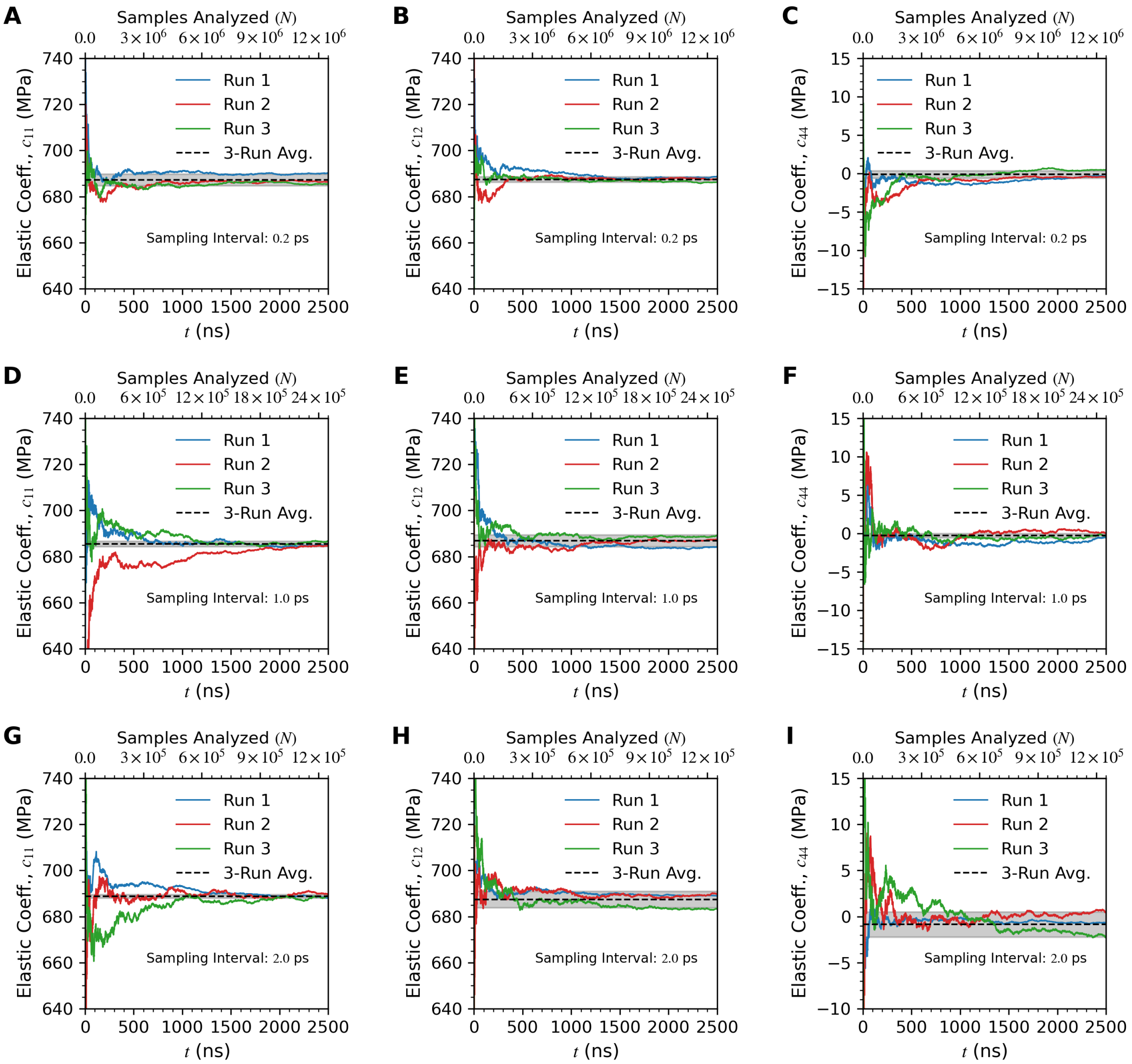

FIG. S6. Convergence of elastic coefficients for CG MARTINI dodecane using different sampling intervals. Top row (A-C) uses a sampling interval of 0.02 ps, middle row (D-F) 0.2 ps, and bottom row (G-I) 1.0 ps. Left panels show c_{11}, middle panels show c_{12}, and right panels show c_{44}. Three independent NVT simulations with different initial conditions were run at each sampling interval shown in blue, red, and green. Dashed black line shows the 3-run average value at the end of the simulations, while the gray shaded region shows the standard deviation.

II. SUPPLEMENTARY TABLES

TABLE S1. Elastic coefficients for solid argon computed using different sampling intervals (Δs) from 3 independent 150 ns simulations.

	$\Delta s = 0.02$ ps	$\Delta s = 1.0$ ps	$\Delta s = 2.0$ ps
c_{11} / MPa	2907 ± 1	2906 ± 3	2905 ± 3
c_{12} / MPa	1642 ± 2	1640 ± 2	1640 ± 5
c_{44} / MPa	1778 ± 1	1778 ± 1	1788 ± 1

TABLE S2. Elastic coefficients for liquid argon computed using different sampling intervals (Δs) from 3 independent 150 ns simulations.

	$\Delta s = 0.02$ ps	$\Delta s = 0.2$ ps	$\Delta s = 1.0$ ps
c_{11} / MPa	323.0 ± 1.3	324.5 ± 1.3	323.3 ± 4.6
c_{12} / MPa	322.5 ± 1.5	323.0 ± 0.9	322.4 ± 2.8
c_{44} / MPa	1.0 ± 0.6	0.74 ± 0.77	0.46 ± 0.51

TABLE S3. Elastic coefficients for MARTINI dodecane computed using different sampling intervals (Δs) from 3 independent 2,500 ns simulations.

	$\Delta s = 0.2$ ps	$\Delta s = 1.0$ ps	$\Delta s = 2.0$ ps
c_{11} / MPa	687.3 ± 2.5	685.5 ± 1.23	688.8 ± 0.8
c_{12} / MPa	687.5 ± 1.2	686.9 ± 2.6	687.4 ± 3.6
c_{44} / MPa	-0.1 ± 0.5	-0.26 ± 0.28	-0.9 ± 1.4

TABLE S4. Elastic coefficients for MARTINI water computed from individual simulations (2,000 ns each) with different integration time-steps (Δt).

	$\Delta t = 0.005$ ps	$\Delta t = 0.01$ ps	$\Delta t = 0.02$ ps	$\Delta t = 0.04$ ps
c_{11} / MPa	924.5 ± 2.7	925.4 ± 1.9	915.2 ± 0.3	885.8 ± 0.3
c_{12} / MPa	921.4 ± 1.1	923.9 ± 0.6	920.7 ± 1.6	914.9 ± 0.7
c_{44} / MPa	-0.8 ± 1.0	-1.3 ± 0.8	-3.0 ± 0.8	-14.7 ± 0.7

III. DERIVATIVES OF TWO AND THREE-BODY POTENTIALS

- Lennard-Jones potential

$$U_{\mathrm{LJ}} = \frac{A_n}{(r^{\alpha\beta})^n} - \frac{B_m}{(r^{\alpha\beta})^m} \tag{1}$$

$$\frac{\partial U_{\mathrm{LJ}}}{\partial r^{\alpha\beta}} = \frac{-nA_n}{(r^{\alpha\beta})^{n+1}} + \frac{mB_m}{(r^{\alpha\beta})^{m+1}} \tag{2}$$

$$\frac{\partial^2 U_{\mathrm{LJ}}}{\partial r^{\alpha\beta}\partial r^{\alpha\beta}} = \frac{(n+1)nA_n}{(r^{\alpha\beta})^{n+2}} - \frac{(m+1)mB_m}{(r^{\alpha\beta})^{m+2}} \tag{3}$$

- Truncated potential at $r^{\alpha\beta} = r_{\mathrm{cut}}$ using a Heaviside function

$$U_{\mathrm{Hcut}} = U(r^{\alpha\beta})\Big(1 - H(r^{\alpha\beta} - r_{\mathrm{cut}})\Big) \tag{4}$$

$$\frac{\partial U_{\mathrm{Hcut}}}{\partial r^{\alpha\beta}} = \left(\frac{\partial U(r^{\alpha\beta})}{\partial r^{\alpha\beta}}\right)\Big(1 - H(r^{\alpha\beta} - r_{\mathrm{cut}})\Big) - U(r^{\alpha\beta})\delta(r^{\alpha\beta} - r_{\mathrm{cut}}) \tag{5}$$

$$\frac{\partial^2 U_{\mathrm{Hcut}}}{\partial r^{\alpha\beta}\partial r^{\alpha\beta}} = \left(\frac{\partial^2 U(r^{\alpha\beta})}{\partial {r^{\alpha\beta}}^2}\right)\Big(1 - H(r^{\alpha\beta} - r_{\mathrm{cut}})\Big) - \frac{\partial U(r^{\alpha\beta})}{\partial r^{\alpha\beta}}\delta(r^{\alpha\beta} - r_{\mathrm{cut}}) \tag{6}$$

- Truncated and shifted potential at $r^{\alpha\beta} = r_{\mathrm{cut}}$ using a Heaviside function

$$U_{\mathrm{HScut}} = \Big(U(r^{\alpha\beta}) - U(r^{\alpha\beta}_{\mathrm{cut}})\Big)\Big(1 - H(r^{\alpha\beta} - r^{\alpha\beta}_{\mathrm{cut}})\Big) \tag{7}$$

$$\frac{\partial U_{\mathrm{HScut}}}{\partial r^{\alpha\beta}} = \left(\frac{\partial U(r^{\alpha\beta})}{\partial r^{\alpha\beta}}\right)\Big(1 - H(r^{\alpha\beta} - r^{\alpha\beta}_{\mathrm{cut}})\Big) + \Big(U(r^{\alpha\beta}_{\mathrm{cut}}) - U(r^{\alpha\beta})\Big)\delta(r^{\alpha\beta} - r^{\alpha\beta}_{\mathrm{cut}}) \tag{8}$$

$$\frac{\partial^2 U_{\mathrm{HScut}}}{\partial r^{\alpha\beta}\partial r^{\alpha\beta}} = \left(\frac{\partial^2 U(r^{\alpha\beta})}{\partial {r^{\alpha\beta}}^2}\right)\Big(1 - H(r^{\alpha\beta} - r^{\alpha\beta}_{\mathrm{cut}})\Big) - \frac{\partial U(r^{\alpha\beta})}{\partial r^{\alpha\beta}}\delta(r^{\alpha\beta} - r^{\alpha\beta}_{\mathrm{cut}}) \tag{9}$$

- Truncated potential with switching function (S_V) from r_{sw} to r_{cut}

$$U_{\mathrm{sw}} = U(r^{\alpha\beta})S_V(r^{\alpha\beta}) \tag{10}$$

$$\frac{\partial U_{\mathrm{sw}}}{\partial r^{\alpha\beta}} = \left(\frac{\partial U(r^{\alpha\beta})}{\partial r^{\alpha\beta}}\right)S_V(r^{\alpha\beta}) + U(r^{\alpha\beta})\left(\frac{\partial S_V(r^{\alpha\beta})}{\partial r^{\alpha\beta}}\right) \tag{11}$$

$$\frac{\partial^2 U_{\mathrm{sw}}}{\partial r^{\alpha\beta}\partial r^{\alpha\beta}} = \left(\frac{\partial^2 U(r^{\alpha\beta})}{\partial r^{\alpha\beta}\partial r^{\alpha\beta}}\right)S_V(r^{\alpha\beta}) + 2\left(\frac{\partial U(r^{\alpha\beta})}{\partial r^{\alpha\beta}}\right)\left(\frac{\partial S_V(r^{\alpha\beta})}{\partial r^{\alpha\beta}}\right) + U(r^{\alpha\beta})\left(\frac{\partial^2 S_V(r^{\alpha\beta})}{\partial r^{\alpha\beta}\partial r^{\alpha\beta}}\right) \tag{12}$$

$$S_V = \frac{1 - 10(r^{\alpha\beta} - r_{\mathrm{sw}})^3(r_{\mathrm{cut}} - r_{\mathrm{sw}})^2 + 15(r^{\alpha\beta} - r_{\mathrm{sw}})^4(r_{\mathrm{cut}} - r_{\mathrm{sw}}) - 6(r^{\alpha\beta} - r_{\mathrm{sw}})^5}{(r_{\mathrm{cut}} - r_{\mathrm{sw}})^5} \tag{13}$$

$$\frac{\partial S_V}{\partial r^{\alpha\beta}} = \frac{-30(r^{\alpha\beta} - r_{\mathrm{sw}})^2(r_{\mathrm{cut}} - r_{\mathrm{sw}})^2 + 60(r^{\alpha\beta} - r_{\mathrm{sw}})^3(r_{\mathrm{cut}} - r_{\mathrm{sw}}) - 30(r^{\alpha\beta} - r_{\mathrm{sw}})^4}{(r_{\mathrm{cut}} - r_{\mathrm{sw}})^5} \tag{14}$$

$$\frac{\partial^2 S_V}{\partial r^{\alpha\beta}\partial r^{\alpha\beta}} = \frac{-60(r^{\alpha\beta} - r_{\mathrm{sw}})(r_{\mathrm{cut}} - r_{\mathrm{sw}})^2 + 180(r^{\alpha\beta} - r_{\mathrm{sw}})^2(r_{\mathrm{cut}} - r_{\mathrm{sw}}) - 120(r^{\alpha\beta} - r_{\mathrm{sw}})^3}{(r_{\mathrm{cut}} - r_{\mathrm{sw}})^5} \tag{15}$$

- Harmonic bond potential

$$U_{\text{har}} = \frac{1}{2}k^b(r^{\alpha\beta} - r_0^{\alpha\beta})^2 \tag{16}$$

$$\frac{\partial U_{\text{har}}}{\partial r^{\alpha\beta}} = k^b(r^{\alpha\beta} - {r_0}^{\alpha\beta}) \tag{17}$$

$$\frac{\partial^2 U_{\text{har}}}{\partial r^{\alpha\beta}\partial r^{\alpha\beta}} = k^b \tag{18}$$

- Harmonic angle potential

$$U_\theta = \frac{1}{2}k^\theta_{\alpha\beta\gamma}(\theta_{\alpha\beta\gamma} - \theta^0_{\alpha\beta\gamma})^2 \tag{19}$$

$$\frac{\partial U_\theta}{\partial r^{\alpha\beta}} = k^\theta_{\alpha\beta\gamma}(\theta_{\alpha\beta\gamma} - \theta^0_{\alpha\beta\gamma})\frac{\partial \theta_{\alpha\beta\gamma}}{\partial r^{\alpha\beta}} \tag{20}$$

$$\frac{\partial^2 U_\theta}{\partial r^{\gamma\epsilon}\partial r^{\alpha\beta}} = k^\theta_{\alpha\beta\gamma}\left[\frac{\partial \theta_{\alpha\beta\gamma}}{\partial r^{\gamma\epsilon}}\frac{\partial \theta_{\alpha\beta\gamma}}{\partial r^{\alpha\beta}} + (\theta_{\alpha\beta\gamma} - \theta^0_{\alpha\beta\gamma})\frac{\partial^2 \theta_{\alpha\beta\gamma}}{\partial r^{\gamma\epsilon}\partial r^{\alpha\beta}}\right] \tag{21}$$

- Harmonic cosine potential

$$U_{\cos} = \frac{1}{2}k_{\alpha\beta\gamma}(\cos(\theta_{\alpha\beta\gamma}) - \cos(\theta^0_{\alpha\beta\gamma}))^2 \tag{22}$$

$$\frac{\partial U_{\cos}}{\partial r^{\alpha\beta}} = k_{\alpha\beta\gamma}(\cos(\theta_{\alpha\beta\gamma}) - \cos(\theta^0_{\alpha\beta\gamma}))\frac{\partial \cos(\theta_{\alpha\beta\gamma})}{\partial r^{\alpha\beta}} \tag{23}$$

$$\frac{\partial^2 U_{\cos}}{\partial r^{\gamma\epsilon}\partial r^{\alpha\beta}} = k_{\alpha\beta\gamma}\left[\frac{\partial \cos(\theta_{\alpha\beta\gamma})}{\partial r^{\gamma\epsilon}}\frac{\partial \cos(\theta_{\alpha\beta\gamma})}{\partial r^{\alpha\beta}} + (\cos(\theta_{\alpha\beta\gamma}) - \cos(\theta^0_{\alpha\beta\gamma}))\frac{\partial^2 \cos(\theta_{\alpha\beta\gamma})}{\partial r^{\gamma\epsilon}\partial r^{\alpha\beta}}\right] \tag{24}$$

- Angle function

$$\theta_{\alpha\beta\gamma} = \cos^{-1}\left(\cos(\theta_{\alpha\beta\gamma})\right) \tag{25}$$

$$\frac{\partial \theta_{\alpha\beta\gamma}}{\partial r^{\alpha\beta}} = \frac{-1}{\sin(\theta_{\alpha\beta\gamma})}\frac{\partial \cos(\theta_{\alpha\beta\gamma})}{\partial r^{\alpha\beta}} \tag{26}$$

$$\frac{\partial^2 \theta_{\alpha\beta\gamma}}{\partial r^{\gamma\epsilon}\partial r^{\alpha\beta}} = \frac{-1}{\sin^3(\theta_{\alpha\beta\gamma})}\left[\frac{\partial^2 \cos(\theta_{\alpha\beta\gamma})}{\partial r^{\gamma\epsilon}\partial r^{\alpha\beta}}(\sin^2(\theta_{\alpha\beta\gamma})) + \frac{\partial \cos(\theta_{\alpha\beta\gamma})}{\partial r^{\gamma\epsilon}}\frac{\partial \cos(\theta_{\alpha\beta\gamma})}{\partial r^{\alpha\beta}}\cos(\theta_{\alpha\beta\gamma})\right] \tag{27}$$

- Cosine function using the law of cosines

$$\cos(\theta_{\alpha\beta\gamma}) = \frac{\boldsymbol{r}^{\alpha\beta} \cdot \boldsymbol{r}^{\beta\gamma}}{\|\boldsymbol{r}^{\alpha\beta}\|\|\boldsymbol{r}^{\beta\gamma}\|} = \frac{(r^{\alpha\beta})^2 + (r^{\beta\gamma})^2 - (r^{\alpha\gamma})^2}{2(r^{\alpha\beta})(r^{\beta\gamma})} \tag{28}$$

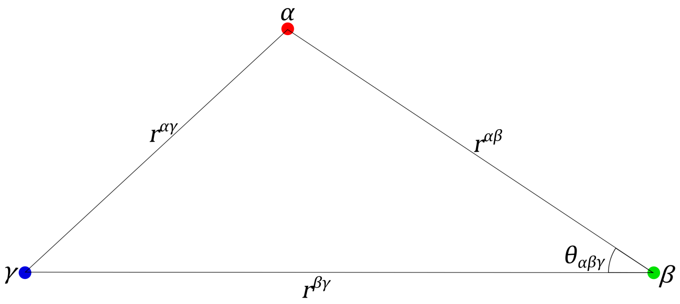

FIG. S7. Illustration of a three-body angle potential acting on particles α, β, and γ based on the angle $\theta_{\alpha\beta\gamma}$.

- Cosine 1st derivatives

$$\frac{\partial \cos(\theta_{\alpha\beta\gamma})}{\partial r^{\alpha\beta}} = \frac{(r^{\alpha\beta})^2 - (r^{\beta\gamma})^2 + (r^{\alpha\gamma})^2}{2(r^{\alpha\beta})^2(r^{\beta\gamma})} \tag{29}$$

$$\frac{\partial \cos(\theta_{\alpha\beta\gamma})}{\partial r^{\beta\gamma}} = \frac{-(r^{\alpha\beta})^2 + (r^{\beta\gamma})^2 + (r^{\alpha\gamma})^2}{2(r^{\alpha\beta})(r^{\beta\gamma})^2} \tag{30}$$

$$\frac{\partial \cos(\theta_{\alpha\beta\gamma})}{\partial r^{\alpha\gamma}} = -\frac{(r^{\alpha\gamma})}{(r^{\alpha\beta})(r^{\beta\gamma})} \tag{31}$$

- Cosine 2nd derivatives

$$\frac{\partial^2 \cos(\theta_{\alpha\beta\gamma})}{\partial r^{\alpha\beta}\partial r^{\alpha\beta}} = \frac{(r^{\beta\gamma})^2 - (r^{\alpha\gamma})^2}{(r^{\alpha\beta})^3(r^{\beta\gamma})} \tag{32}$$

$$\frac{\partial^2 \cos(\theta_{\alpha\beta\gamma})}{\partial r^{\beta\gamma}\partial r^{\alpha\beta}} = \frac{\partial^2 \cos(\theta_{\alpha\beta\gamma})}{\partial r^{\alpha\beta}\partial r^{\beta\gamma}} = -\frac{(r^{\alpha\beta})^2 + (r^{\beta\gamma})^2 + (r^{\alpha\gamma})^2}{2(r^{\alpha\beta})^2(r^{\beta\gamma})^2} \tag{33}$$

$$\frac{\partial^2 \cos(\theta_{\alpha\beta\gamma})}{\partial r^{\alpha\gamma}\partial r^{\alpha\beta}} = \frac{\partial^2 \cos(\theta_{\alpha\beta\gamma})}{\partial r^{\alpha\beta}\partial r^{\alpha\gamma}} = \frac{(r^{\alpha\gamma})}{(r^{\alpha\beta})^2(r^{\beta\gamma})} \tag{34}$$

$$\frac{\partial^2 \cos(\theta_{\alpha\beta\gamma})}{\partial r^{\beta\gamma}\partial r^{\beta\gamma}} = \frac{(r^{\alpha\beta})^2 - (r^{\alpha\gamma})^2}{(r^{\alpha\beta})(r^{\beta\gamma})^3} \tag{35}$$

$$\frac{\partial^2 \cos(\theta_{\alpha\beta\gamma})}{\partial r^{\alpha\gamma}\partial r^{\beta\gamma}} = \frac{\partial^2 \cos(\theta_{\alpha\beta\gamma})}{\partial r^{\beta\gamma}\partial r^{\alpha\gamma}} = \frac{(r^{\alpha\gamma})}{(r^{\alpha\beta})(r^{\beta\gamma})^2} \tag{36}$$

$$\frac{\partial^2 \cos(\theta_{\alpha\beta\gamma})}{\partial r^{\alpha\gamma}\partial r^{\alpha\gamma}} = \frac{-1}{(r^{\alpha\beta})(r^{\beta\gamma})} \tag{37}$$